

1 **Spatiotemporal forecast of extreme events in a chaotic** 2 **dynamical model of slow slip events**

3 Hojjat Kaveh^{1*}, Jean Philippe Avouac², Andrew M Stuart³

¹ *Mechanical and Civil Engineering, California Institute of Technology, Pasadena, CA, USA*

² *Geology and Planetary Science, California Institute of Technology, Pasadena, CA, USA*

³ *Computing and Mathematical Science, California Institute of Technology, Pasadena, CA, USA*

4 **SUMMARY**

5
6 Seismic and aseismic slip events result from episodic slips on faults and are often chaotic due
7 to stress heterogeneity. Their predictability in nature is a widely open question. In this study,
8 we forecast extreme events in a numerical model. The model, which consists of a single fault
9 governed by rate-and-state friction, produces realistic sequences of slow events with a wide
10 range of magnitudes and inter-event times. The complex dynamics of this system arise from
11 partial ruptures. As the system self-organizes, the state of the system is confined to a chaotic
12 attractor of a relatively small dimension. We identify the instability regions within this attrac-
13 tor where large events initiate. These regions correspond to the particular stress distributions
14 that are favorable for near complete ruptures of the fault. We show that large events can be
15 forecasted in time and space based on the determination of these instability regions in a low-
16 dimensional space and the knowledge of the current slip rate on the fault.

17 **Key words:**

18 Seismic cycle – Self-organization – Earthquake interaction, forecasting, and prediction – Numerical
19 modelling

* orresponding author; E-mail: hkaveh@caltech.edu.

20 **1 INTRODUCTION**

21 Earthquakes and Slow Slip Events (SSEs) result from episodic frictional slip on the faults. Each
22 slip event releases the elastic strain accumulated during an interevent period during which the
23 fault is locked. This principle is often referred to as the elastic rebound theory in reference to Reid
24 (1910). While the elastic rebound theory offers valuable insights into the long-term mean recur-
25 rence time of earthquakes and can be used for time-independent earthquake forecasting (Avouac,
26 2015; Marsan & Tan, 2020), it falls short of predicting the time or the magnitude of the larger
27 events (Murray & Segall, 2002). The difficulty is that earthquakes often exhibit a chaotic be-
28 havior which is manifest in the irregular and rare occurrence of large slip events and various
29 empirical scaling laws, such as the Gutenberg-Richter and the Omori laws (Scholz, 1989). The
30 Gutenberg-Richter law (Gutenberg & Richter, 1950) states that earthquake magnitudes are dis-
31 tributed exponentially (the number of earthquakes with magnitude larger than M , $N(M)$, is given
32 by $\log_{10} N(M) = a - bM$, where b is a scaling parameter of the order of one and a is a constant).
33 The Omori law (Utsu et al., 1995) states that the rate of earthquakes during an aftershock sequence
34 decays as $1/t$ where t is the time since the mainshock. Chaotic behavior has also been identified in
35 sequences of SSEs in Cascadia (Gualandi et al., 2020). These events obey the same scaling laws
36 as regular earthquakes and produce very similar crack-like and pulse-like ruptures, although with
37 several orders of magnitudes smaller slip rate and stress drop (Michel et al., 2019).

38 The main source of complexities in earthquake sequences is due to stress heterogeneities which
39 can either be of static origin (due to fault geometry (Okubo & Aki, 1987), roughness (Sagy et al.,
40 2007; Cattania, 2019), or heterogeneity of mechanical properties (Kaneko et al., 2010)) or dy-
41 namic, due stress transfers among faults or within a single fault (Shaw & Rice, 2000). As the
42 stress evolves during the earthquake cycle, it generates asperities and barriers that can either facil-
43 itate a complete rupture of a fault (a system-size rupture) or impede the propagation of a rupture,
44 resulting in a partial rupture. Partial or complete ruptures of a fault system are therefore observed
45 in nature (Konca et al., 2008). Large ruptures, though rare according to the Gutenberg-Richter law,
46 hold greater significance from a seismic hazard perspective.

47 Advances in the understanding of fault friction (Marone, 1998) and in numerical modeling of

48 earthquake sequences (Rice, 1993; Lapusta et al., 2000; Lapusta & Liu, 2009) now make it possible to produce realistic simulations (Barbot et al., 2012). When performing those numerical simulations, initial conditions cannot be any arbitrary value, and it is also crucial to recognize that certain initial conditions hold more statistical relevance than others during the evolution of the dynamical system. For example, Lapusta & Rice (2003) and Rubin & Ampuero (2005) advocate for conducting simulations over multiple seismic cycles to mitigate the influence of arbitrary choices in initial conditions. In fact, the space of feasible stress distributions on a fault during earthquake cycles is significantly smaller than the space of arbitrary initial conditions, as the dynamical system self-organizes into a chaotic attractor (Shaw & Rice, 2000). When a dynamical system converges to its chaotic attractor, any state outside this attractor is not feasible within the system's evolution. Consequently, the space of feasible states is limited to the attractor itself, resulting in a significantly smaller domain compared to the space of any arbitrary states for the system.

60 Large events happen rarely in the chaotic evolution of the earthquake cycle so their forecast is extremely challenging. We hypothesize that as for other types of dynamical systems that produce extreme (or rare) events (Blonigan et al., 2019; Farazmand & Sapsis, 2019), the trajectory of the dynamical system must traverse specific instability regions within the chaotic attractor for large fault ruptures to occur. These instability regions correspond to the optimal distributions of stress (or the states of the frictional interface) that facilitate large ruptures and are also accessible during the evolution of the system because they are part of the chaotic attractor. Despite considerable research on deterministic chaos in earthquake cycle models (Huang & Turcotte, 1990; Becker, 2000; Anghel et al., 2004; Kato, 2016; Barbot, 2019), certain essential features of the chaotic attractor, particularly modes relevant to instability that are also statistically feasible, have remained elusive in the literature. This is primarily due to the high-dimensional, chaotic, and multi-scale nature of the problem, as well as the rarity of large events.

72 The identification of the optimal state of the frictional interface that promotes large events, out of all the statistically feasible distributions is the primary focus of this study. Following the approach of (Farazmand & Sapsis, 2017), we use an approximation of the chaotic attractor of the system during the inter-event period; this approximation uses Proper Orthogonal Decomposition (POD)

76 to reduce dimension and account for the feasibility constraint. Representing the optimal state of
 77 the frictional interface in a low dimensional space is favorable for the purpose of earthquake fore-
 78 casting, as the data to constrain the physical parameters and current states of the system are sparse
 79 for earthquake cycles. We use the proximity of the current slip rate of the system to the slip rates
 80 of optimal solutions to propose an effective forecast method of large events. Our results suggest
 81 that this framework can be used to predict events in both space and time when we have access to
 82 the slip rate on the fault with certain resolution.

83 As our case study, we use a quasi-dynamic model with the standard rate-and-state friction with the
 84 aging law (Ruina, 1983). We apply this methodology to a 2D fault within a 3D medium, using a
 85 model setup analog to a model that has been shown to produce a realistic sequence of SSEs similar
 86 to those observed in Cascadia (Dal Zilio et al., 2020). We limit the analysis to the case of SSEs as
 87 in that case a quasi-dynamic approximation is justified which speeds up the numerical simulations
 88 (Rice, 1993; Thomas et al., 2014). The complexity of events (and in particular the frequency of
 89 small events) has been shown to depend on the ratio of the fault length (or width) to the nucleation
 90 size (Barbot, 2019; Cattania, 2019). We benefit from the fact that SSEs have a much larger ratio
 91 of nucleation size to the size of the fault compared to regular earthquakes. The range of magnitude
 92 of events in our 1000 years of synthetic data is 5.6-7.4 whereas for a large fault system with typ-
 93 ical earthquakes, the range is much bigger. Spatially small-scale processes in regular earthquakes
 94 contribute to more complexity of the system. This might limit the applicability of our method to
 95 these events without any further considerations.

96 **2 MODEL SET UP**

97 We use a quasi-dynamic model of slip events on a 2D fault in a 3D elastic medium, assuming
 98 rate-and-state friction with the aging law for the evolution of the state variable (θ):

$$\frac{\tau}{\bar{\sigma}_n} = \mu^{ref} + a \ln\left(\frac{V}{V^{ref}}\right) + b \ln\left(\frac{\theta V^{ref}}{D_{RS}}\right), \quad (1a)$$

$$\frac{d\theta}{dt} = 1 - \frac{\theta V}{D_{RS}}. \quad (1b)$$

99 Here, $V((x, y), t) : \Gamma \times \mathbb{R}^+ \rightarrow \mathbb{R}^+$ is slip rate on the fault, $\theta((x, y), t) : \Gamma \times \mathbb{R}^+ \rightarrow \mathbb{R}^+$ is

100 the state variable, $\tau((x, y), t) : \Gamma \times \mathbb{R}^+ \rightarrow \mathbb{R}^+$ is the frictional strength, $\bar{\sigma}_n$ is the effective normal
 101 stress, and a, b, D_{RS} are frictional properties of the surface (Γ) and are positive. μ^{ref} and V^{ref} are
 102 reference friction and slip rate respectively. The sign of $a - b$ determines the frictional regime of the
 103 fault. For $a - b > 0$, the fault is Velocity Strengthening (VS); a jump in the velocity would increase
 104 the fault strength. Regions with $a - b > 0$ suppress the rupture nucleation and acceleration. For
 105 $a - b < 0$ fault is Velocity Weakening (VW); a jump in the slip rate (V) and slipping more than
 106 D_{RS} , decrease the strength, and the fault is capable of nucleating earthquakes and accelerating the
 107 ruptures. $a - b$ varies spatially and is plotted in Fig 1(a).

108 The stress rate on the fault can also be written as:

$$\dot{\tau} = \mathcal{L}(V - V_{pl}) - \frac{G}{2c_s}\dot{V}, \quad (2)$$

109 where \mathcal{L} is a pseudo-differential operator, and contains elastostatic response (Geubelle & Rice,
 110 1995), and V_{pl} is the plate slip rate. G and c_s are shear modulus and shear wave speed respectively.
 111 By taking the time derivative of Eq (1a), and eliminating $\dot{\tau}$ using Eq (2), we have a dynamical
 112 system for $u = [V, \theta]^\top$. One can also use other pairs of variables such as $[V, \tau]^\top$ to describe this
 113 dynamical system.

114 In practice, we consider a planar thrust fault with 90° dip angle in elastic half-space that consists
 115 of a Velocity-Weakening (VW) patch (dotted area in Fig 1 (a)), within which ruptures can nucle-
 116 ate and propagate, surrounded by a Velocity-Strengthening (VS) patch where the propagation of
 117 seismic ruptures is inhibited (Fig 1 (a)). The fault is loaded by a surrounding fault that slips at a
 118 constant rate.

119 The model, with the properly selected and piece-wise constant parameters and initial conditions,
 120 exhibits a complex sequence of events with a variety of magnitudes distributed with a heavy tail
 121 consistent with the Gutenberg-Richter law (Fig 1 (b)). The shear stress on the locked portion of
 122 the fault (Fig 1 (c)) increases during the interevent period, leading to elastic strain energy build-
 123 up. During episodic slip events, the shear stress drops, and elastic strain energy is released and
 124 dissipated by frictional sliding and the radiation damping (Fig 1 (c)). To justify the assumption
 125 of ignoring wave propagation effects along the fault, we choose a parameter regime that produces

126 SSEs in which V is small enough that the wave effects across the faults are negligible. The model
 127 parameters are taken from (Dal Zilio et al., 2020) to simulate SSEs similar to those in Cascadia.
 128 For simplicity we did not include the effect of pore-pressure dilatancy. The frictional and physical
 129 properties of our problem are summarized in Table 1 and Fig 1.

130 The time series of the sequence of partial rupture with rare large ruptures is plotted in Fig 1 (c,d).
 131 Since stress is a function of θ and V in the rate-and-state friction, and θ is not measurable, we do
 132 not have access to stress distribution directly. As a result, in this work, we only assume that we
 133 have observations of the current slip rate when performing extreme event forecasting. In practice,
 134 the current slip rate on the fault can be indirectly constrained by measurements of ground surface
 135 displacements which involves an inversion that greatly reduces the spatial resolution of slip rate.
 136 Therefore, we will also examine a simplified low-resolution slip rate measurement to mimic the
 137 limitations of real observations and assess the performance of our algorithm under such condi-
 138 tions. The slip potency deficit, which is the difference between the slip potency (integral of slip
 139 on the fault) and the slip potency if the fault was uniformly slipping at the loading rate, is plotted
 140 to show the chaotic behavior of the system and the rare occurrence of large events. The potency
 141 deficit builds up during the interevent period and drops during the episodic slip events (Fig 1 (e)).
 142 The time series of the magnitude of events is also plotted in Fig 1 (f). The maximum slip rate on
 143 the fault is plotted in Fig 2 with the dashed line as the threshold that we use for defining an event.

144 3 EXTREME EVENTS FORECASTING METHODS

145 3.1 Extreme events formulation

146 The dynamical system that comes from combining Eq 1 and 2 describes the coupled evolution of
 147 two functions $V((x, y), t) : \Gamma \times \mathbb{R}^+ \rightarrow \mathbb{R}^+$ and $\theta((x, y), t) : \Gamma \times \mathbb{R}^+ \rightarrow \mathbb{R}^+$. We assume $u = [V, \theta]^\top$
 148 belongs to an appropriately chosen function space $\mathcal{U} : (\Gamma \times \mathbb{R}^+) \times (\Gamma \times \mathbb{R}^+) \rightarrow \mathbb{R}^+ \times \mathbb{R}^+$ and
 149 characterizes the state of the frictional interface at any given time and position on the fault. In
 150 the context of rate-and-state friction, shear stress is a function of the combination of variables
 151 (V, θ) . Also, the evolution of the system is better rendered in the $\log_{10} u$ space. Consequently,
 152 we use the term ‘pre-event state’ to refer to the spatial distribution of $w = [\log_{10} V, \log_{10} \theta]^\top$

153 before a rupture; nonetheless, we formulate the dynamical model in terms of $u = (V, \theta)$. To avoid
 154 confusion between the term ‘state’ as used to describe the system’s condition before an event
 155 and the ‘state variable’ in the friction law, we clarify that ‘pre-event state’ refers to the overall
 156 system configuration, $w = [\log_{10} V, \log_{10} \theta]^\top$, prior to the event. Meanwhile, the ‘state variable’
 157 (θ) specifically denotes the internal variable in the rate-and-state friction law.

158 The dynamical system for u is both multi-scale and chaotic and produces ruptures with a variety
 159 of sizes. The governing equation is

$$\frac{\partial u}{\partial t} = \mathcal{N}(u) \quad (3a)$$

$$u(x, y, 0) = u_0(x, y), \quad \forall (x, y) \in \Gamma \quad (3b)$$

160 where \mathcal{N} is a nonlinear differential operator[†] that encompasses the quasi-dynamic approximation
 161 of the elastodynamics and the friction law (Eqs 1 and 2). We denote S^t as the solution operator for
 162 the dynamical system, mapping the current state forward by t time-units:

$$u(x, y, t) = S^t(u(x, y, 0)); \quad (4)$$

163 we can break this map into the components S_V^t and S_θ^t :

$$S^t(u(x, y, 0)) = [S_V^t(u(x, y, 0)), S_\theta^t(u(x, y, 0))]^\top \quad (5)$$

164 We assume that the dynamical system has a global attractor \mathcal{A} on which the dynamics are chaotic;
 165 we refer to this as the chaotic attractor in what follows.

166 Inspired by (Farazmand & Sapsis, 2019), we define event set $E(V_{\text{thresh}})$ for a prescribed thresh-
 167 old $V_{\text{thresh}} \in \mathbb{R}^+$ as:

$$E(V_{\text{thresh}}) = \{u \in \mathcal{U} : \sup_{(x,y) \in \Gamma} V(x, y) \geq V_{\text{thresh}}\} \quad (6)$$

168 By setting a proper event threshold (V_{thresh}), the event set includes both partial and full ruptures.

169
 170 We now seek to determine the optimal feasible distributions of $\log_{10} u$ (pre-event state) in the
 171 interevent period that for a prediction horizon T lead to large magnitude events. By a ‘feasible

[†] Technically a pseudo-differential operator

pre-event state’, we mean a state that is inside the chaotic attractor of the system; a combination of V and θ that is likely to be realized during the evolution of the dynamical system. We also want our criteria for optimality of ‘pre-event state’ to be low-dimensional so that it can be captured using observations that are typically sparse in reality. We then use our low-dimensional critical pre-event state and only the current measurable state of the system (slip rate, which can in principle be estimated from geodetic measurements) to forecast the time and location of a possible large event in a time window horizon.

To formulate the question in mathematical terms, we introduce the moment magnitude of fault slip cumulated over the duration of integration Δt .

$$\widetilde{M}(u(x, y, t); \Delta t) = \frac{2}{3} \log_{10} \left(G \int_0^{\Delta t} \int_{\Gamma} S_V^{t'}(u(x, y, t)) dx dy dt' \right) - 6. \quad (7)$$

where G is the elastic shear modulus. \widetilde{M} measures the seismic moment on the fault in the \log_{10} scale during Δt time-units (Scholz, 1989). \widetilde{M} is slightly different from the definition of the moment magnitude (M) for one event because in \widetilde{M} , we take Δt to be a constant rather than being the actual duration of a particular event. In practice, we set it to be larger than the longest duration of events in our model. While we make use of \widetilde{M} in our problem setup and benefit from its continuity over u , we will report the performance of the forecast of extreme events with a regular definition of moment magnitude (M).

We next define a cost function:

$$F(u; \Delta t, T) = \sup_{t \in [0, T]} \widetilde{M}(S^t(u); \Delta t) \quad (8)$$

where function $F : \mathcal{U} \rightarrow \mathbb{R}$ takes u as input and, for a prescribed prediction horizon (T) and event duration (Δt), finds the largest moment magnitude generated by the initial condition u . The optimal (most dangerous) feasible pre-event state conditions are determined by finding the local maxima (U^*) of $F(u; \Delta t, T)$ over $u \in \mathcal{A} \setminus E(V_{\text{thresh}})$ through an optimization process:

$$U^* = \{u^* | u^* \in \mathcal{A} \setminus E(V_{\text{thresh}}), u^* \text{ is a local maximizer of } F(u; \Delta t, T), F(u^*; \Delta t, T) > F_e^*\} \quad (9)$$

where F_e^* is some threshold for the magnitude to define a ‘large’ event. Eq (9) encompasses the main question of this work; that is finding optimal and statistically feasible pre-event state on

195 the fault during the interevent period that makes large events in a short time window. In Eq (9),
 196 $u^* \in \mathcal{A} \setminus E(V_{\text{thresh}})$ ensures that u^* is inside the chaotic attractor (statistical feasibility constraint)
 197 and also in the interevent period; any state (u^*) outside \mathcal{A} is inaccessible during the system's
 198 evolution because of the self-organization. After solving the optimization problem (Eq (9)), we
 199 use the 'similarity' of the current states of the system to solutions of Eq (9), as an indicator of
 200 an upcoming large event. We use the current slip rate as our only knowledge of the current state
 201 of the system as θ is not measurable. Solutions to Eq (9) are instability regions inside the chaotic
 202 attractor that generate large ruptures within the time span of $[0, T]$.

203 Set $\mathcal{A} \setminus E(V_{\text{thresh}})$ is a complicated set in the high-dimensional function space \mathcal{U} . Even if we can
 204 solve this optimization problem in this large space, it would be impractical to represent pre-event
 205 state in this high-dimensional space because the sparse data generally available in reality can only
 206 yield a low-dimensional model of the slip rate distribution on a fault. As a result, we approximate
 207 this set with a simpler set, characterized in a low-dimensional space using the POD method. This
 208 approach is developed in the next part.

209 3.2 Model reduction and forecast scheme

210 Many high-dimensional chaotic dynamical systems can be approximated by a low-dimensional
 211 system (Taira et al., 2017; Rowley & Dawson, 2017; Li et al., 2023; Brandstätter et al., 1983).
 212 Although the underlying dynamics of earthquakes and Slow Slip cycles are often chaotic (Huang &
 213 Turcotte, 1990; Becker, 2000; Anghel et al., 2004; Kato, 2016; Barbot, 2019), in certain examples,
 214 it has been observed that the chaotic attractors are low dimensional (Gualandi et al., 2020,0) which
 215 mathematically implies that we can approximate the evolution of the sequence of events using
 216 parameters in a finite-dimensional space instead of an infinite-dimensional function space. We
 217 use this property to reduce the dimensionality and approximate the chaotic attractor during the
 218 interevent period.

219 We approximate and reduce the dimensionality of the chaotic attractor of the system during the
 220 inter-event period using the POD technique (explained in Appendix A). The POD approach is
 221 widely adopted in the study of turbulent fluid flow (Taira et al., 2017); it is a linear model reduction

method that uses singular value decomposition on a dataset of snapshot time series of the field, with the time-average removed. This process identifies spatial modes that are ranked according to their statistical significance in the dataset. Since the evolution of the system is better realized in the $w = \log_{10} u$ space, we apply the POD on the w rather than u . We denote by \bar{w} the time average of the field (w) during the interevent period. POD technique inputs snapshots of $w - \bar{w}$ during the interevent period and gives orthonormal basis functions $\phi_i : \Gamma \times \Gamma \rightarrow \mathbb{R} \times \mathbb{R}$ and their associated variance λ_i for $i \geq 1$ where $\lambda_1 > \lambda_2 > \dots$ which quantifies the statistical importance of each mode in the dataset. The subtraction of the mean is crucial because it ensures that the covariance matrix in the POD algorithm accurately reflects the variability and relationships within the dataset, rather than being influenced by the absolute positions of the data points. Then we can describe w , and consequently u , using a new coordinate system with the basis functions defined by ϕ_i 's. Since the basis functions are ordered by the variance they capture in the data, the truncation and approximation of the field $w - \bar{w}$, with the first N_m POD modes captures a maximal statistical relevance (in the variance sense) of data between all possible N_m dimensional linear subspaces of $\log_{10} \mathcal{U}$.

We approximate $w : w \in \log_{10} (\mathcal{A} \setminus E(V_{\text{thresh}}))$ as perturbations around the time-average of w during the interevent period ($\bar{w} = [\bar{w}^V, \bar{w}^\theta]$) along those basis functions. Since we want to approximate only the interevent period we should exclude the event period ($E(V_{\text{thresh}})$) from the dataset of snapshots that are used to find POD modes (ϕ_i 's). Following Blonigan et al. (2019), we constrain the perturbations along those eigenvectors to lie within a hyperellipse with a radius along each eigenvector proportional to the standard deviation of the data captured by each mode. In other words, we allow more perturbation along those directions that capture more statistical relevance in the data. The approximation of the chaotic attractor during the interevent period can be written as:

$$\log_{10} (\mathcal{A} \setminus E(V_{\text{thresh}})) \approx \left\{ \bar{w} + \sum_{i=1}^{N_m} a_i \phi_i \mid \sum_{i=1}^{N_m} \frac{a_i^2}{\lambda_i} \leq r_0^2 \right\}. \quad (10)$$

where ϕ_i 's ($i \geq 1$) are the orthonormal basis functions ordered by the data variance they capture (λ_i) in the centered dataset of time snapshots of $w - \bar{w}$ excluding the event period $E(V_{\text{thresh}})$. Here

248 a_i is the amplitude of perturbation along ϕ_i and N_m is the number of basis functions we keep in
 249 our model reduction. The maximum perturbation along each basis function (ϕ_i) is constrained by
 250 the corresponding variance λ_i . One can play with the amplitude of the allowed perturbation which
 251 is represented by r_0 .

252 Then Eq (9), which is an optimization problem in a high-dimensional function space \mathcal{U} , con-
 253 strained on a complicated set $\mathcal{A} \setminus E(V_{\text{thresh}})$, can be approximated as an optimization problem
 254 in a low-dimensional (\mathbb{R}^{N_m}) space constrained within a hyperellipse. To solve the constrained
 255 optimization problem, we use optimal sampling in the framework of Bayesian optimization as
 256 it is useful when the objective function is costly to evaluate (Blanchard & Sapsis, 2021). The
 257 optimization method is described in Appendix B. Alternative approaches, such as adjoint-based
 258 optimization methods, can also be employed to enhance the efficiency of solving the optimiza-
 259 tion problem (Stiernström et al., 2024; Blonigan et al., 2019). During the optimization process,
 260 we collect all optimal pre-event states ($w^* = [(\log V)^*, (\log \theta)^*]^\top$) in a set W^* that satisfies the
 261 feasibility constraint ($w^* \in \log_{10}(\mathcal{A} \setminus E(V_{\text{thresh}}))$) and has the value of $F(10^{w^*}; \Delta t, T)$ above the
 262 threshold F_e^* :

$$263 \quad W^* := \left\{ w^* = \bar{w} + \sum_{i=1}^{N_m} a_i \phi_i \mid \sum_{i=1}^{N_m} \frac{a_i^2}{\lambda_i} \leq r_0^2, F(10^{w^*}; \Delta t, T) > F_e^* \right\}. \quad (11)$$

264 W^* corresponds to the set of all of the pre-event states leading to extreme events. To perform the
 265 spatial forecast, we need to record the evolution of each w^* for up to time T .

266 We use the proximity of the current state of the system to optimal states as an indicator of an
 267 upcoming large event. The current state of the system (w) is not measurable because θ is not
 268 measurable. Slip rate is the measurable component in w and we use it as a proxy of the current
 269 state of the system. Then, following Blonigan et al. (2019), we use the maximum cosine similarity
 270 between the \log_{10} of the current slip rate ($\log V(t)$) and all of the optimal slip rates ($\log V_i^*$'s) in
 271 the set W^* as an indicator that signals an upcoming large event.

$$I(t) = \max_i \frac{\langle \log V(t) - \bar{w}^V, \log V_i^* - \bar{w}^V \rangle_{L^2}}{\| \log V(t) - \bar{w}^V \|_2 \| \log V_i^* - \bar{w}^V \|_2} \quad (12)$$

272 where $\langle \cdot, \cdot \rangle_{L^2}$ is the L^2 inner product, \bar{w}^V is the average slip rate during interevent periods in the
 273 dataset, $\log V_i^*$ is the velocity component of the i^{th} optimal pre-event state (w_i^*), and $\| \cdot \|_2$ is the
 274 L^2 norm. Note that $I(t)$ is only a function of the current slip rate on the fault.

275 4 RESULTS

276 4.1 Extreme event forecast

277 We use a simulation run for a total duration of 2200 years. We exclude the initial 200 years to elim-
 278 inate the transient behavior, letting the system converge to its chaotic attractor. To define the event
 279 set (Eq (6)), we set the event threshold $V_{\text{thresh}} = 5 \times 10^{-8} (m/s)$. The event threshold is chosen
 280 such that we get reasonable scaling properties and also, don't lose many events. The time series of
 281 the maximum slip velocity on the fault is plotted in Fig 2 in which V_{thresh} is denoted by a dashed
 282 line. We use data from $t = 200$ to $t = 1200$ years to perform the model reduction and find basis
 283 functions ϕ_i 's and their corresponding variances λ_i 's. We approximate $\mathcal{A} \setminus E(V_{\text{thresh}})$ using Eq
 284 (10) with a number of modes $N_m = 13$ which capture more than 85% variance of the data (based
 285 on the discussion in Appendix A). The mean of the field ($\bar{w} = [\bar{w}^V, \bar{w}^\theta]^\top$) together with the first
 286 four eigenfunctions $\phi_i = [\phi_i^V, \phi_i^\theta]^\top$ for interevent periods for the time range $t \in [200, 1200]$ (year)
 287 are plotted in Fig (3) with \bar{w} as the empirical mean of the interevent states of the system w , ϕ_i^V as
 288 the i^{th} eigenfunction of the $\log_{10} V$ and ϕ_i^θ as the i^{th} eigenfunction of the $\log_{10} \theta$. Using ϕ_i 's and
 289 λ_i 's, we solve the optimization problem which has T (prediction horizon), Δt (event duration),
 290 and r_0 (amount of perturbation around \bar{w}) as hyper-parameters. We set the prediction horizon to
 291 $T = 0.5(\text{year})$ and $\Delta t = 0.25(\text{year})$ as the maximum duration of events in the time window
 292 of $t \in [200, 1200]$ year. With the increase of T , because of the effect of chaos, the predictability
 293 decreases and we would expect the performance of the algorithm to decrease.

294 The value of r_0 in the Eq (10) controls the size of the hyperellipse which is the constraint of the
 295 optimization problem. We perform the optimization for different values of r_0 (in Appendix B).
 296 For perturbations constrained within a small hyperellipse (small r_0), the algorithm does not find
 297 any optimal pre-event state that leads to a large event. This makes sense because, for small r_0 , w
 298 is close to the \bar{w} which is the average state of w during interevent periods. For very large r_0 , the

299 approximation of $\mathcal{A} \setminus E(V_{\text{thresh}})$ with a hyperellipse is less valid because we let the perturbation
 300 have amplitudes much larger than the standard deviation of each component along each eigen-
 301 function. So, one should find an intermediate r_0 whose values of the cost function at the local
 302 maxima are larger but close to the maximum magnitude observed in the dataset. Here, we report
 303 results for $r_0 = 3$ which means that we don't let the pre-event state go outside the total 3 standard
 304 deviation range from \bar{w} in \mathbb{R}^{N_m} . Unlike Blonigan et al. (2019) that, for a fluid flow problem, found
 305 a unique solution for their similar optimization problem, we see convergence to multiple local
 306 maxima ($w^* = [(\log V)^*, (\log \theta)^*]^\top$) for different algorithm initiations. As a result, to make our
 307 algorithm robust, we solve the optimization problem multiple times with random initiations.

308 The average stress during the interevent period for the VW patch, and the prestress corresponding
 309 to one of the optimal solutions is plotted in Fig 4 (a,b). We have also plotted the dimensionless
 310 quantity $\log_{10}(V\theta/D_{RS})$ in Fig 4 (c). The term $V\theta/D_{RS}$ indicates whether the fault is above or
 311 below steady state in the rate-and-state friction law. When $V\theta/D_{RS} > 1$, the fault is above steady
 312 state, signaling the nucleation phase, while $V\theta/D_{RS} < 1$ means the fault is below steady state,
 313 in a healing phase (Rubin & Ampuero, 2005). The cumulative slip distribution corresponding to
 314 the event with magnitude 7.5 led by the optimal pre-event state is plotted in Fig 4 (d). We have
 315 plotted the slip rate (V), and the state variable (θ) corresponding to this particular optimal solu-
 316 tion, together with the convergence of the optimization algorithm, in Appendix B. We record the
 317 rupture extent of optimal solutions (a total of 12 local maxima) that have $F_e^* > 7.4$ to use for
 318 spatial prediction. These optimal pre-event state distributions are relatively complex with hetero-
 319 geneities both along the strike and along the dip directions. Because we have only approximated
 320 the chaotic attractor by a hyperellipse, the solutions of the optimization problem are unlikely to
 321 be exactly observed in the simulation of the dynamical system evolution. However, when initiat-
 322 ing from sufficiently close points within the chaotic attractor, the trajectories remain close together
 323 during the early stages of their evolution. We rely on this principle to forecast the time and location
 324 of large slip events. It is interesting to note that with the defined event threshold, we don't see any
 325 full-system size rupture in the forward simulation. However, if we start from homogeneous initial
 326 conditions, we see periodic fault-size ruptures. This solution is probably unstable or stable with

327 a small basin of attraction because a relatively small perturbation from the homogeneous initial
 328 condition leads to the convergence of the system to its chaotic attractor.

329 The indicator $I(t)$ (Eq (12)), can effectively forecast large events for the dataset from $t = 1200$ to
 330 $t = 2200$ years with a prediction horizon of $T = 0.5$ (year). To illustrate, $I(t)$ is plotted alongside
 331 F in Fig 5 (a). A high value of F shows an upcoming large event in the time interval $[0, T]$ and we
 332 observe that when F rises, the indicator signals a large event by rising to large values. We define
 333 a threshold I_e above which we signal an upcoming large event. We also define F_e as the threshold
 334 for extreme events; whenever F is larger than F_e we say that an extreme event is going to happen
 335 in the next T year(s). The values of F_e and I_e are determined such that the proportion of the true
 336 positive and true negative forecasts of extreme events are maximized. By recording the values of
 337 $I(t)$ and $F(t)$, we can empirically find the conditional probability $P(F|I)$ (Fig 5 (b)). Values of F_e
 338 and I_e are denoted by the white vertical and horizontal dashed lines in Fig 5 (b). The probability
 339 in this context is with respect to the invariant measure of the chaotic attractor. Different quadrants
 340 of this plot show four conditions including true negative, false negative, true positive, and false
 341 positive from bottom left counterclockwise to top left. While most of the high values of $P(F|I)$
 342 lie inside the true negative and true positive regions, it is essential to acknowledge that the proba-
 343 bilities of false negative and false positive are not zero. We also plot the empirical probability of
 344 observing an event greater than F_e given the knowledge of I , ($P[F > F_e|I]$). This value which
 345 is denoted by P_{ee} is plotted in Fig 5 (c). P_{ee} consistently rises to values close to one, which is
 346 another way to show that the indicator I can be used as a predictor of large events. We plot the
 347 forecast of rupture extent in Fig 5 (d) which shows the effectiveness of both spatial and temporal
 348 forecasts of large events. Since we have recorded the rupture extent of optimal solutions (elements
 349 in set W^*), as soon as the current state of the system gets close to the i^{th} optimal solution and the
 350 indicator signals an upcoming event ($I(t) > I_e$), we propose the recorded rupture extent of the
 351 i^{th} optimal solution as the spatial forecast. Fig 5 (e) shows the temporal forecast of events with the
 352 magnitude of events plotted in blue. Whenever the indicator has a value greater than I_e , we fore-
 353 cast (red region) that an event larger than $F_e = 6.9$ (black dashed line) will happen. Red shows the
 354 temporal prediction of events larger than F_e . The magnitude in Fig 5 (e) is calculated according

355 to the regular definition of the magnitude of an event (i.e. by integrating the slip velocity above
 356 the threshold over the exact duration of the event). In Supplemental Video 1, an animation of this
 357 prediction is available.

358 4.2 Forecast with Partial Observation of Slip Rate

359 So far, we have assumed that we have full access to the slip rate on the fault. Here, we relax this
 360 assumption and use slip rate measurements only at a few points on the fault (diamonds in Fig 1
 361 (a)). We denote $\hat{V} : \mathbb{R}^{N_p} \times \mathbb{R}^+ \rightarrow \mathbb{R}^+$ as the time series of partial slip rate observation, where
 362 N_p is the number of points of slip rate measurements and we take it to be 16 in this case study.
 363 We assume that these points are at the center of the fault along the depth and have equal distances
 364 along the strike. We redefine the indicator $I(t)$ for this special case as follows:

$$I(t) = \max_i \frac{\langle \log \hat{V}(t) - \hat{w}^V, \log \hat{V}_i^* - \hat{w}^V \rangle_{\mathbb{R}^{N_p}}}{\| \log \hat{V}(t) - \hat{w}^V \|_2 \| \log \hat{V}_i^* - \hat{w}^V \|_2} \quad (13)$$

365 where \hat{V}_i^* is the slip rate at the measurement points (diamonds in Fig 1 (a)) of the i^{th} optimal
 366 solution in the set W^* . \hat{w}^V is the average slip rate at the measurement points during the interevent
 367 period. $\langle \cdot, \cdot \rangle_{\mathbb{R}^{N_p}}$ is the inner product in \mathbb{R}^{N_p} . Fig 6 shows the forecast performance in the limited slip
 368 rate measurement scenario. The general consistent increase in $I(\cdot)$ when the function $F(\cdot)$ rises is
 369 visible in Fig 6 (a). Fig 6 (b) and (c) show statistically the performance of the predictor. While most
 370 of the probability mass of $P(F|I)$ belongs to true positive and true negative we should appreciate
 371 that there is more probability mass in the false positive quadrant compared to the scenario in which
 372 we have full access to the slip rate. This can be observed better in Fig 6 (c), (d), and (e). Although
 373 as I increases, P_{ee} increases consistently, P_{ee} is almost 0.9 when I is the maximum which suggests
 374 that there is a 10% chance of a false positive signal when I takes its maximum value. This false
 375 positive can also be observed in Fig 6 (d) and (e) around the year 1610. While it is important
 376 to appreciate the limitations, the overall performance is satisfying. To reduce this limitation, one
 377 can use filtering methods to invert and approximate slip rates at a few more points on the fault to
 378 improve the performance.

4.3 Impact of low resolution observation on prediction accuracy

In this part, we illustrate a limitation of our method as we lose more and more information with loosing the resolution of the data. Real-world slip inversion on the fault has inherent low-pass filter because the process of finding slip on the fault from surface displacements involves filtering techniques that inevitably introduce this type of limitation. These techniques are necessary due to the measurement limitations, which cannot capture high-frequency variations accurately, leading to a smoother and potentially less precise representation of the actual slip rates. We apply a Gaussian kernel to the synthetic slip rate data, mimicking the characteristics of realistic datasets. This approach enables us to systematically assess the impact of reduced resolution in the observed slip rate on the performance of extreme event prediction. By varying the standard deviation of the Gaussian kernel, we evaluate how different resolutions affect the algorithm's accuracy. The standard deviation is expressed in a dimensionless form relative to the width of the VW zone.

We assume that the slip rate is corrupted by a Gaussian kernel which is defined mathematically as:

$$G(x, y) = \frac{1}{2\pi\sigma^2} \exp\left(-\frac{x^2 + y^2}{2\sigma^2}\right). \quad (14)$$

where σ is the standard deviation of the Gaussian kernel, controlling the extent of the smoothing effect. By convolving this kernel with the original slip rate data $V(x, y)$, we obtain the low resolution slip rate $V'(x, y)$:

$$V'(x, y) = \int_{\Gamma} V(x', y') \cdot G(x - x', y - y') dx' dy' \quad (15)$$

To visually demonstrate the effect of the kernel on the data, we plotted one snapshot of slip rate without applying the low-pass filter in Fig 7 (a) and then applied the low-pass filter with different standard deviation on that snapshot of the velocity and plot them in Fig 7 (b,c,d). The conditional probability $P(F|I)$ for a 1000-year-long data that are corrupted by these Gaussian kernels are plotted in Fig 7 (e,f,g). As the resolution decreases the probability mass in the upper left (false positive) and lower right (false negative) increases. Fig 7 (f) and (g) show that with a standard deviation greater than $0.5W_{VW}$, we have a large probability of a false signal. This is a limitation of our work and potentially considering more POD modes, using data assimilation techniques to

403 more accurately invert for slip on the fault, and considering the history of the time series are some
 404 of the methods that can be used to improve the performance when the slip rate on the fault is not
 405 well constrained.

406 5 DISCUSSION

407 Our results demonstrate the possibility of predicting the time, size, and spatial extent of extreme
 408 events in a simplified dynamical model of earthquake sequences based on the instantaneous ob-
 409 servation of fault slip rate. By constraining the pre-event state on a fault to the only feasible ones
 410 and solving an optimization problem, we found the optimal pre-event state in a low dimensional
 411 space. Optimal pre-event state refers to configurations of slip rate and state variable heterogeneity
 412 on the fault triggering large events within small time windows. Identifying the optimal pre-event
 413 state distributions that are also statistically accessible during the earthquake cycle is pivotal.

414 States of the system self-organize into a chaotic attractor which occupies only a small fraction of
 415 all possible distributions on the fault. The identification of the optimal pre-event state within this
 416 reduced set is crucial for two reasons. First, it helps establish a low-dimensional representation of
 417 optimal pre-event state; the significance of reduced-order proxy of critical pre-event state is even
 418 more important for earthquakes than SSEs, primarily due to the scarcity of observational data ob-
 419 tained from paleoseismic records. Second, everything outside this set remains unseen during the
 420 earthquake cycle's evolution. If that was not the case, the space of hypothetical stress distribution
 421 possibly leading to large events would be intractable.

422 In section 4.2, we studied a scenario in which the slip rate is known at only a few points on the fault.
 423 The results are almost as good as when we have full access to the slip rate on the fault because the
 424 slip evolution at neighboring points on the fault is strongly correlated due to elastic coupling. This
 425 result most likely benefits from large nucleation length for SSEs which is generally not true for
 426 earthquakes. The nucleation length for a 1D fault for mode III is given by $h_{ra} = \frac{2GD_{RS}b}{\pi\bar{\sigma}(b-a)^2}$ (Rubin &
 427 Ampuero, 2005), where G is shear modulus, $\bar{\sigma}$ is the effective normal stress, and a, b, D_{RS} are fric-
 428 tional parameters. For a 2D fault, the nucleation size is given by $h = (\pi^2/4)h_{ra}$ (Chen & Lapusta,
 429 2009), and is $29.7(km)$ in our model, whereas the width of the VW zone is $W_{VW} = 25(km)$.

430 Slip rate data of a fault is determined through the inversion of surface displacement, which results
431 in low spatial resolution. We therefore studied the performance of extreme event prediction when
432 the synthetic slip rate is corrupted by a low pass filter. Our results Fig 7 indicate that predictability
433 is compromised when the standard deviation of the low-pass filter kernel gets larger and larger.
434 This finding highlights a limitation in the application of our study in its current form when the slip
435 rate on the fault is not well resolved. Addressing this limitation will be a focus of our future work.
436 Potential approaches include incorporating additional components into the extreme event criteria
437 and solving a data assimilation problem, such as using the Ensemble Kalman filter, to more accu-
438 rately invert for slip rates on the fault.

439 For earthquakes, the ratio of the nucleation size to fault dimensions is much smaller than in SSEs.
440 Rupture dynamics considerations indicate that the initial shear stress must be sufficiently high and
441 well-correlated across the entire fault for a system-spanning earthquake to occur. Therefore, hav-
442 ing information at least at the scale of the fault dimension is essential to predict *whether* a big
443 rupture will happen. However, to predict when the event will nucleate, it might be necessary to re-
444 solve the system at the scale of the nucleation length, as constraints on the slip rate at this scale are
445 crucial. A key question remains: for earthquakes, is resolving the system at the nucleation length
446 scale necessary for time predictability, and is resolution at the fault dimension sufficient to predict
447 the extent of rupture? Investigating the role of observational resolution in the predictability of both
448 the timing and extent of future seismic events remains a significant challenge, which we aim to
449 address in future works.

450 **6 CONCLUSION**

451 Our study suggests that the chaotic nature of earthquake sequences is not an insurmountable ob-
452 stacle to time-dependent earthquake forecasting. However, we acknowledge that we considered a
453 favorable model setup designed to produce SSEs. It would be now interesting to test this approach
454 in the case of a model setup producing regular earthquakes (i.e., with slip rates of $1\text{cm}/\text{s}$ to $1\text{m}/\text{s}$
455 to be comparable to real earthquakes) with larger ratios of fault dimensions to nucleation size and
456 with a larger range of earthquake magnitudes (Barbot, 2021; Cattania, 2019; Lambert & Lapusta,

2021). This is doable although computationally challenging. The amplitude of the stress heterogeneity would be more substantial for regular earthquakes, where dynamic wave-mediated stresses allow for rupture propagation over lower stress conditions than for aseismic slip, particularly in models with stronger dynamic weakening or with persistent heterogeneity such as normal stress perturbations.(Noda et al., 2009; Lambert et al., 2021).

It is expected that earthquake sequences would then show more complexity due to the cascading effects which are responsible for foreshocks and aftershocks in natural earthquake sequences, and which are not present in our simulations. In that regard, Blonigan et al. (2019) reported that the performance of their prediction of rare events diminishes with the increase in Reynolds number in their turbulent flow case. It is possible that we have the same limitation as the ratio of the nucleation size to the dimensions of the fault decreases.

ACKNOWLEDGMENTS

The authors HK and J-PA express their sincere gratitude to the National Science Foundation (NSF) for their financial support of this research project, through the Industry-University Collaborative Research Center Geomechanics and Mitigation of Geohazards (award #1822214). Author AMS is grateful to DoD for support as a Vannevar Bush Faculty Fellow. Additionally, the authors are grateful for the valuable input and discussion provided by Nadia Lapusta, Brendan Meade, Themis Sapsis, Adriano Gualandi, Alba Rodriguez, Camilla Cattania, Elif Oral, Mateo Acosta, Kelian Dascher-Cousineau, Zachary R Ross, Jan Dirk Jansen, Kyungjae Im. The authors also extend their appreciation to Eric Dunham and the other anonymous reviewer for their constructive feedback and insightful comments.

Data Availability Statement

We used a model of a 2D thrust fault in a 3D medium governed by rate-and-state friction with aging law for the evolution of state variable (θ). The model parameters are summarized in Table 1. To

481 simulate the forward model, we use the [QDYN software](#)[‡], which is an open-source code to simulate
482 earthquake cycles (Luo et al., 2017). We use the POD technique to reduce the dimensionality of the
483 problem. This method is reviewed in Appendix A. To solve the optimization problem we use the
484 Bayesian optimization method (Brochu et al., 2010; Blanchard & Sapsis, 2021) that is reviewed
485 in Appendix B. We used the open source code available on [GitHub](#)[§] for solving the optimization
486 problem.

487 **Supplementary Materials**

488 Supplemental Videos: Movie S1 to Movie S2

[‡] <https://github.com/ydluo/qdyn>

[§] <https://github.com/ablancha/gpsearch>

489 **References**

- 490 Anghel, M., Ben-Zion, Y., & Rico-Martinez, R., 2004. Dynamical System Analysis and Fore-
 491 casting of Deformation Produced by an Earthquake Fault, in *Computational Earthquake Science*
 492 *Part I*, Pageoph Topical Volumes, pp. 2023–2051, eds Donnellan, A., Mora, P., Matsu'ura, M.,
 493 & Yin, X.-c., Birkhäuser, Basel.
- 494 Avouac, J.-P., 2015. From Geodetic Imaging of Seismic and Aseismic Fault Slip to Dynamic
 495 Modeling of the Seismic Cycle, *Annual Review of Earth and Planetary Sciences*, **43**(1), 233–
 496 271, _eprint: <https://doi.org/10.1146/annurev-earth-060614-105302>.
- 497 Barbot, S., 2019. Slow-slip, slow earthquakes, period-two cycles, full and partial ruptures, and
 498 deterministic chaos in a single asperity fault, *Tectonophysics*, **768**, 228171.
- 499 Barbot, S., 2021. A Spectral Boundary-Integral Method for Quasi-Dynamic Ruptures of Multiple
 500 Parallel Faults, *Bulletin of the Seismological Society of America*, **111**(3), 1614–1630.
- 501 Barbot, S., Lapusta, N., & Avouac, J.-P., 2012. Under the Hood of the Earthquake Machine:
 502 Toward Predictive Modeling of the Seismic Cycle, *Science*, **336**(6082), 707–710, Publisher:
 503 American Association for the Advancement of Science.
- 504 Becker, T. W., 2000. Deterministic Chaos in two State-Variable Friction Sliders and the Effect of
 505 Elastic Interactions, in *Geocomplexity and the Physics of Earthquakes*, pp. 5–26, American Geo-
 506 physical Union (AGU), _eprint: <https://onlinelibrary.wiley.com/doi/pdf/10.1029/GM120p0005>.
- 507 Blanchard, A. & Sapsis, T., 2021. Bayesian optimization with output-weighted optimal sampling,
 508 *Journal of Computational Physics*, **425**, 109901.
- 509 Blonigan, P. J., Farazmand, M., & Sapsis, T. P., 2019. Are extreme dissipation events predictable
 510 in turbulent fluid flows?, *Physical Review Fluids*, **4**(4), 044606, Publisher: American Physical
 511 Society.
- 512 Brandstätter, A., Swift, J., Swinney, H. L., Wolf, A., Farmer, J. D., Jen, E., & Crutchfield, P. J.,
 513 1983. Low-Dimensional Chaos in a Hydrodynamic System, *Physical Review Letters*, **51**(16),
 514 1442–1445, Publisher: American Physical Society.
- 515 Brochu, E., Cora, V. M., & de Freitas, N., 2010. A Tutorial on Bayesian Optimization of Expensive
 516 Cost Functions, with Application to Active User Modeling and Hierarchical Reinforcement

- 517 Learning, arXiv:1012.2599 [cs].
- 518 Cattania, C., 2019. Complex Earthquake Sequences On Simple
519 Faults, *Geophysical Research Letters*, **46**(17-18), 10384–10393, _eprint:
520 <https://onlinelibrary.wiley.com/doi/pdf/10.1029/2019GL083628>.
- 521 Chen, T. & Lapusta, N., 2009. Scaling of small repeating earthquakes explained by interaction
522 of seismic and aseismic slip in a rate and state fault model, *Journal of Geophysical Research:*
523 *Solid Earth*, **114**(B1), _eprint: <https://onlinelibrary.wiley.com/doi/pdf/10.1029/2008JB005749>.
- 524 Dal Zilio, L., Lapusta, N., & Avouac, J., 2020. Unraveling Scaling Properties of Slow-Slip
525 Events, *Geophysical Research Letters*, **47**(10).
- 526 Farazmand, M. & Sapsis, T. P., 2017. A variational approach to probing extreme events in tur-
527 bulent dynamical systems, *Science Advances*, **3**(9), e1701533, Publisher: American Association
528 for the Advancement of Science.
- 529 Farazmand, M. & Sapsis, T. P., 2019. Extreme Events: Mechanisms and Prediction, *Applied*
530 *Mechanics Reviews*, **71**(5).
- 531 Geubelle, P. H. & Rice, J. R., 1995. A spectral method for three-dimensional elastodynamic
532 fracture problems, *Journal of the Mechanics and Physics of Solids*, **43**(11), 1791–1824.
- 533 Gualandi, A., Avouac, J.-P., Michel, S., & Faranda, D., 2020. The predictable chaos of slow
534 earthquakes, *Science Advances*, **6**(27), eaaz5548, Publisher: American Association for the Ad-
535 vancement of Science.
- 536 Gualandi, A., Faranda, D., Marone, C., Cocco, M., & Mengaldo, G., 2023. Deterministic and
537 stochastic chaos characterize laboratory earthquakes, *Earth and Planetary Science Letters*, **604**,
538 117995.
- 539 Gutenberg, B. & Richter, C. F., 1950. Seismicity of the Earth and associated phenomena,
540 *MAUSAM*, **1**(2), 174–176, Number: 2.
- 541 Huang, J. & Turcotte, D. L., 1990. Are earthquakes an example of de-
542 terministic chaos?, *Geophysical Research Letters*, **17**(3), 223–226, _eprint:
543 <https://onlinelibrary.wiley.com/doi/pdf/10.1029/GL017i003p00223>.
- 544 Kaneko, Y., Avouac, J.-P., & Lapusta, N., 2010. Towards inferring earthquake patterns from

- 545 geodetic observations of interseismic coupling, *Nature Geoscience*, **3**(5), 363–369, Number: 5
546 Publisher: Nature Publishing Group.
- 547 Kato, N., 2016. Earthquake Cycles in a Model of Interacting Fault Patches: Complex Behavior
548 at Transition from Seismic to Aseismic Slip, *Bulletin of the Seismological Society of America*,
549 **106**(4), 1772–1787.
- 550 Konca, A. O., Avouac, J.-P., Sladen, A., Meltzner, A. J., Sieh, K., Fang, P., Li, Z., Galetzka, J.,
551 Genrich, J., Chlieh, M., Natawidjaja, D. H., Bock, Y., Fielding, E. J., Ji, C., & Helmberger, D. V.,
552 2008. Partial rupture of a locked patch of the Sumatra megathrust during the 2007 earthquake
553 sequence, *Nature*, **456**(7222), 631–635, Number: 7222 Publisher: Nature Publishing Group.
- 554 Lambert, V. & Lapusta, N., 2021. Resolving Simulated Sequences of Earthquakes
555 and Fault Interactions: Implications for Physics-Based Seismic Hazard Assessment,
556 *Journal of Geophysical Research: Solid Earth*, **126**(10), e2021JB022193, _eprint:
557 <https://onlinelibrary.wiley.com/doi/pdf/10.1029/2021JB022193>.
- 558 Lambert, V., Lapusta, N., & Faulkner, D., 2021. Scale Dependence of Earthquake Rupture Pre-
559 stress in Models With Enhanced Weakening: Implications for Event Statistics and Inferences of
560 Fault Stress, *Journal of Geophysical Research: Solid Earth*, **126**(10), e2021JB021886, _eprint:
561 <https://onlinelibrary.wiley.com/doi/pdf/10.1029/2021JB021886>.
- 562 Lapusta, N. & Liu, Y., 2009. Three-dimensional boundary integral modeling of sponta-
563 neous earthquake sequences and aseismic slip, *Journal of Geophysical Research: Solid Earth*,
564 **114**(B9), _eprint: <https://onlinelibrary.wiley.com/doi/pdf/10.1029/2008JB005934>.
- 565 Lapusta, N. & Rice, J. R., 2003. Nucleation and early seismic propagation of small and large
566 events in a crustal earthquake model, *Journal of Geophysical Research: Solid Earth*, **108**(B4),
567 _eprint: <https://onlinelibrary.wiley.com/doi/pdf/10.1029/2001JB000793>.
- 568 Lapusta, N., Rice, J. R., Ben-Zion, Y., & Zheng, G., 2000. Elastodynamic analysis for slow
569 tectonic loading with spontaneous rupture episodes on faults with rate- and state-dependent
570 friction, *Journal of Geophysical Research: Solid Earth*, **105**(B10), 23765–23789, _eprint:
571 <https://onlinelibrary.wiley.com/doi/pdf/10.1029/2000JB900250>.
- 572 Li, M., Jain, S., & Haller, G., 2023. Model reduction for constrained mechanical systems via

- 573 spectral submanifolds, *Nonlinear Dynamics*, **111**(10), 8881–8911.
- 574 Luo, Y., Ampuero, J. P., Galvez, P., Ende, M. v. d., & Idini, B., 2017. QDYN: a Quasi-DYNamic
575 earthquake simulator (v1.1).
- 576 Marone, C., 1998. Laboratory-Derived Friction Laws and Their Application to Seis-
577 mic Faulting, *Annual Review of Earth and Planetary Sciences*, **26**(1), 643–696, _eprint:
578 <https://doi.org/10.1146/annurev.earth.26.1.643>.
- 579 Marsan, D. & Tan, Y. J., 2020. Maximum Earthquake Size and Seismicity Rate from an ETAS
580 Model with Slip Budget, *Bulletin of the Seismological Society of America*, **110**(2), 874–885.
- 581 Michel, S., Gualandi, A., & Avouac, J.-P., 2019. Similar scaling laws for earthquakes and Casca-
582 dia slow-slip events, *Nature*, **574**(7779), 522–526, Number: 7779 Publisher: Nature Publishing
583 Group.
- 584 Murray, J. & Segall, P., 2002. Testing time-predictable earthquake recurrence by direct measure-
585 ment of strain accumulation and release, *Nature*, **419**(6904), 287–291, Number: 6904 Publisher:
586 Nature Publishing Group.
- 587 Noda, H., Dunham, E. M., & Rice, J. R., 2009. Earthquake ruptures with thermal weakening and
588 the operation of major faults at low overall stress levels, *Journal of Geophysical Research: Solid
589 Earth*, **114**(B7), _eprint: <https://onlinelibrary.wiley.com/doi/pdf/10.1029/2008JB006143>.
- 590 Okubo, P. G. & Aki, K., 1987. Fractal geometry in the San Andreas Fault
591 System, *Journal of Geophysical Research: Solid Earth*, **92**(B1), 345–355, _eprint:
592 <https://onlinelibrary.wiley.com/doi/pdf/10.1029/JB092iB01p00345>.
- 593 Reid, H., 1910. *The Mechanics of the Earthquake, The California Earthquake of April 18, 1906,*
594 *Report of the State Investigation Commission*, vol. 2.
- 595 Rice, J. R., 1993. Spatio-temporal complexity of slip on a fault, *Jour-
596 nal of Geophysical Research: Solid Earth*, **98**(B6), 9885–9907, _eprint:
597 <https://onlinelibrary.wiley.com/doi/pdf/10.1029/93JB00191>.
- 598 Rowley, C. W. & Dawson, S. T., 2017. Model Reduction for Flow Analysis and Control, *An-
599 nual Review of Fluid Mechanics*, **49**(1), 387–417, _eprint: [https://doi.org/10.1146/annurev-fluid-
600 010816-060042](https://doi.org/10.1146/annurev-fluid-010816-060042).

- 601 Rubin, A. M. & Ampuero, J.-P., 2005. Earthquake nucleation on (aging) rate
602 and state faults, *Journal of Geophysical Research: Solid Earth*, **110**(B11), [_eprint:
603 https://onlinelibrary.wiley.com/doi/pdf/10.1029/2005JB003686](https://onlinelibrary.wiley.com/doi/pdf/10.1029/2005JB003686).
- 604 Ruina, A., 1983. Slip instability and state variable friction laws, *Jour-
605 nal of Geophysical Research: Solid Earth*, **88**(B12), 10359–10370, [_eprint:
606 https://onlinelibrary.wiley.com/doi/pdf/10.1029/JB088iB12p10359](https://onlinelibrary.wiley.com/doi/pdf/10.1029/JB088iB12p10359).
- 607 Sagy, A., Brodsky, E. E., & Axen, G. J., 2007. Evolution of fault-surface roughness with slip,
608 *Geology*, **35**(3), 283–286.
- 609 Scholz, C. H., 1989. *Mechanics of faulting*, Publication Title: Annual review of earth and plane-
610 tary sciences. Vol. 17 ISSN: 0084-6597.
- 611 Shaw, B. E. & Rice, J. R., 2000. Existence of continuum complexity in the elastodynamics of
612 repeated fault ruptures, *Journal of Geophysical Research: Solid Earth*, **105**(B10), 23791–23810,
613 [_eprint: https://onlinelibrary.wiley.com/doi/pdf/10.1029/2000JB900203](https://onlinelibrary.wiley.com/doi/pdf/10.1029/2000JB900203).
- 614 Stiernström, V., Almquist, M., & Dunham, E. M., 2024. Adjoint-based inversion for stress and
615 frictional parameters in earthquake modeling, arXiv:2310.12279 [cs, math].
- 616 Taira, K., Brunton, S. L., Dawson, S. T. M., Rowley, C. W., Colonius, T., McKeon, B. J., Schmidt,
617 O. T., Gordeyev, S., Theofilis, V., & Ukeiley, L. S., 2017. Modal Analysis of Fluid Flows: An
618 Overview, *AIAA Journal*, **55**(12), 4013–4041, Publisher: American Institute of Aeronautics and
619 Astronautics.
- 620 Thomas, M. Y., Lapusta, N., Noda, H., & Avouac, J.-P., 2014. Quasi-dynamic versus fully
621 dynamic simulations of earthquakes and aseismic slip with and without enhanced coseis-
622 mic weakening, *Journal of Geophysical Research: Solid Earth*, **119**(3), 1986–2004, [_eprint:
623 https://onlinelibrary.wiley.com/doi/pdf/10.1002/2013JB010615](https://onlinelibrary.wiley.com/doi/pdf/10.1002/2013JB010615).
- 624 Utsu, T., Ogata, Y., S, R., & Matsu'ura, 1995. The Centenary of the Omori Formula for a Decay
625 Law of Aftershock Activity, *Journal of Physics of the Earth*, **43**(1), 1–33.

Table 1. Physical Properties

VW region	a	0.004
	b	0.014
VS region	a	0.019
	b	0.014
Characteristic slip weakening distance	D_{RS}	0.045(m)
Reference steady state slip rate	V^{ref}	$10^{-6} \frac{m}{s}$
Reference steady-state friction coefficient	μ^{ref}	0.6
Effective normal stress	$\bar{\sigma}_n$	10(MPa)
Shear modulus	G	30(GPa)
Plate loading Velocity	V_{pl}	40(mm/year)

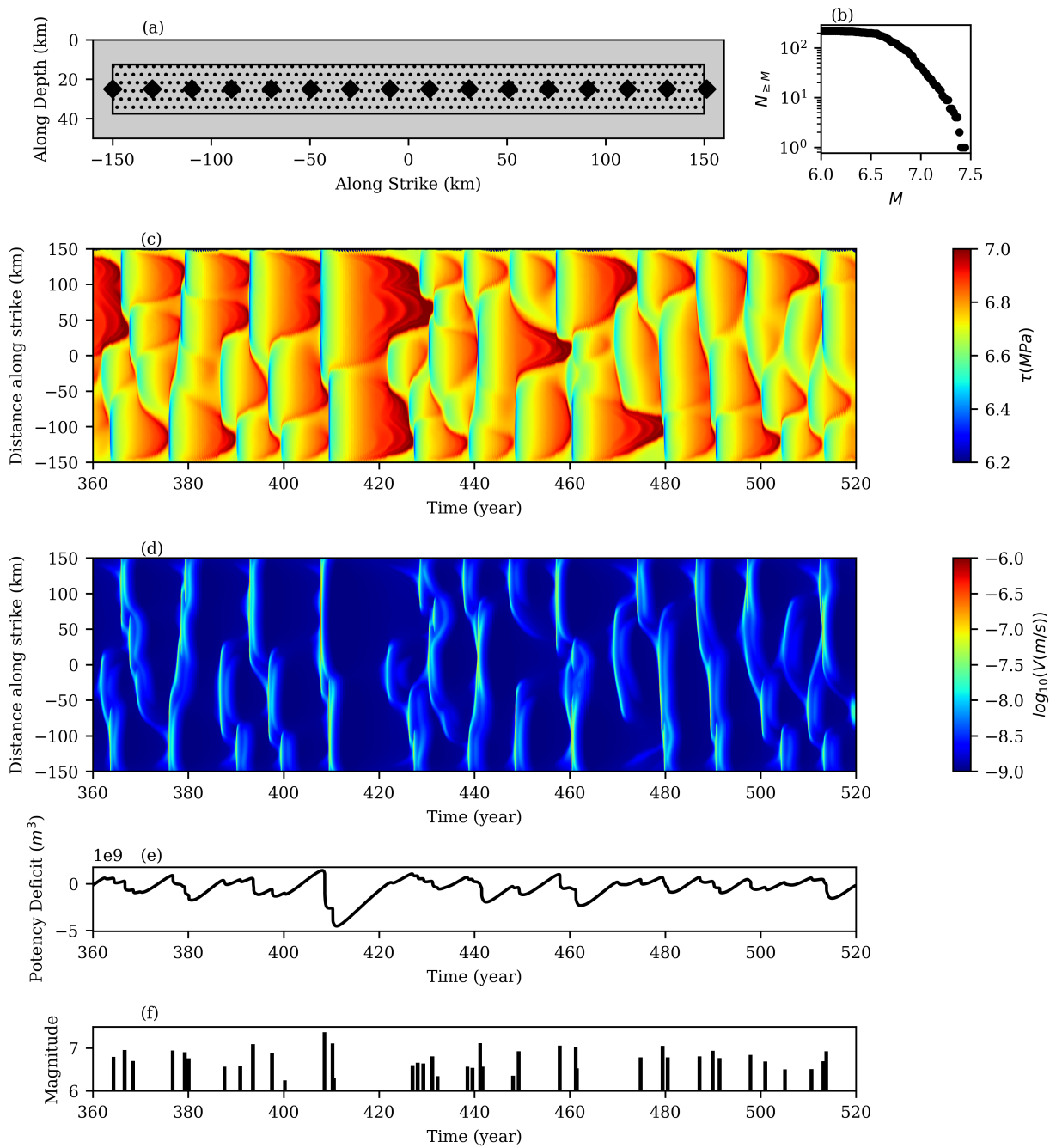


Figure 1. Geometry of the fault (a). The VW patch is the dotted area that is surrounded by the VS patch. The diamonds are the locations of slip rate measurements for the scenario in which we do not have full access to the slip rate on the entire fault. The number of events with a magnitude greater than M , (N_M) is plotted in (b) for 1000 years of simulation time. Maximum stress along the depth for the VW patch is plotted as a function of distance along strike and time (c). The maximum slip rate for the VW patch along the depth is plotted as a function of distance along strike and time (d). The time-series of the potency deficit and magnitudes are plotted in (e) and (f) respectively.

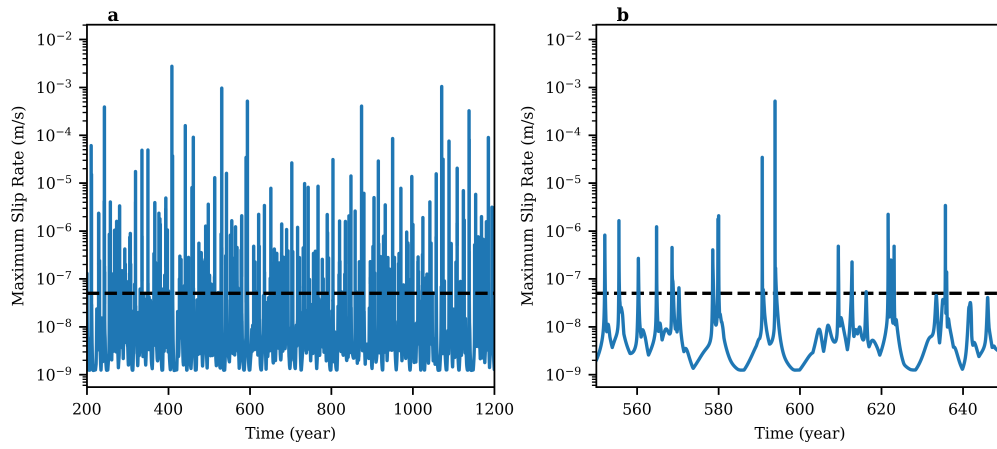


Figure 2. Time series of the maximum slip rate for a period of 1000 years (a) and 100 years (b) with threshold velocity denoted by a dashed line.

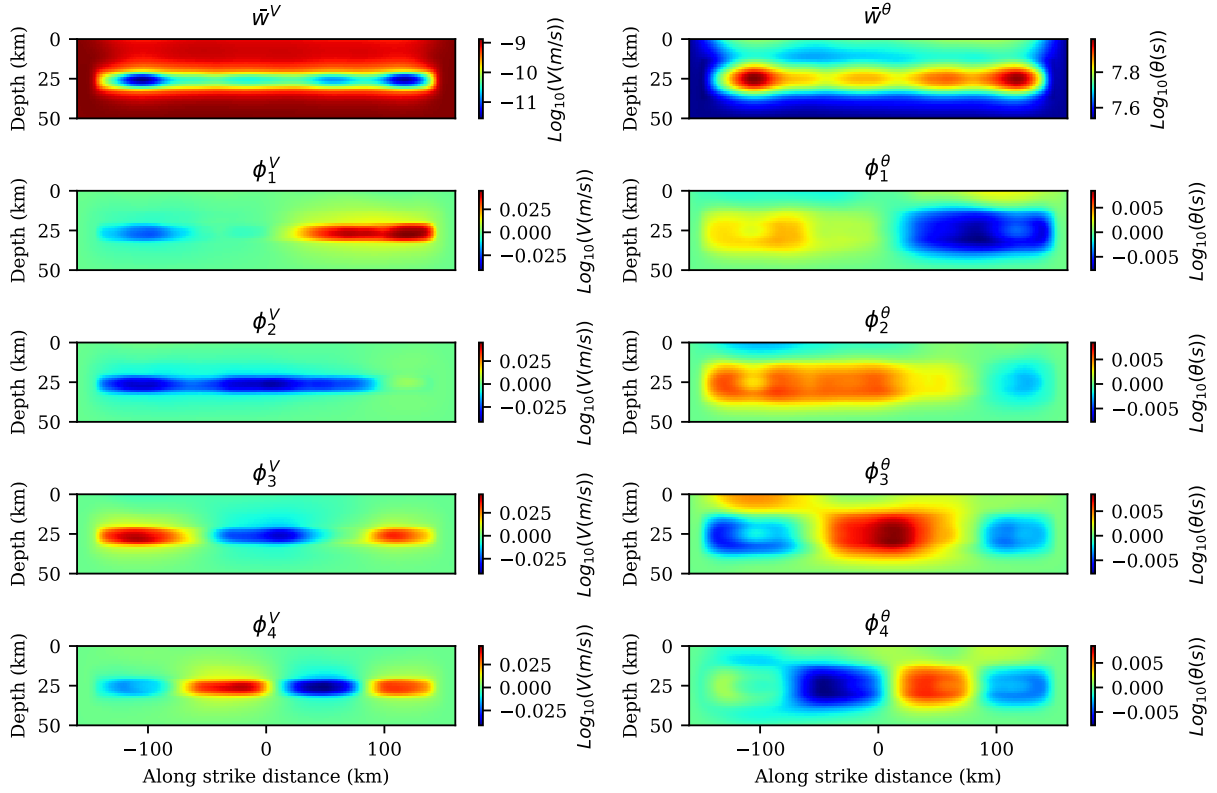


Figure 3. Average of the \log_{10} of slip rate (\bar{w}^V) and state variable (\bar{w}^θ) during the interevent periods, and first four eigenfunctions for \log_{10} of slip rate (ϕ_i^V for $1 \leq i \leq 4$) and state variable (ϕ_i^θ for $1 \leq i \leq 4$) that are ordered by the variance they capture in the datasets. The dataset contains interevent snapshots of \log_{10} of slip rate and state variable during the interevent periods from the year 200 to 1200.

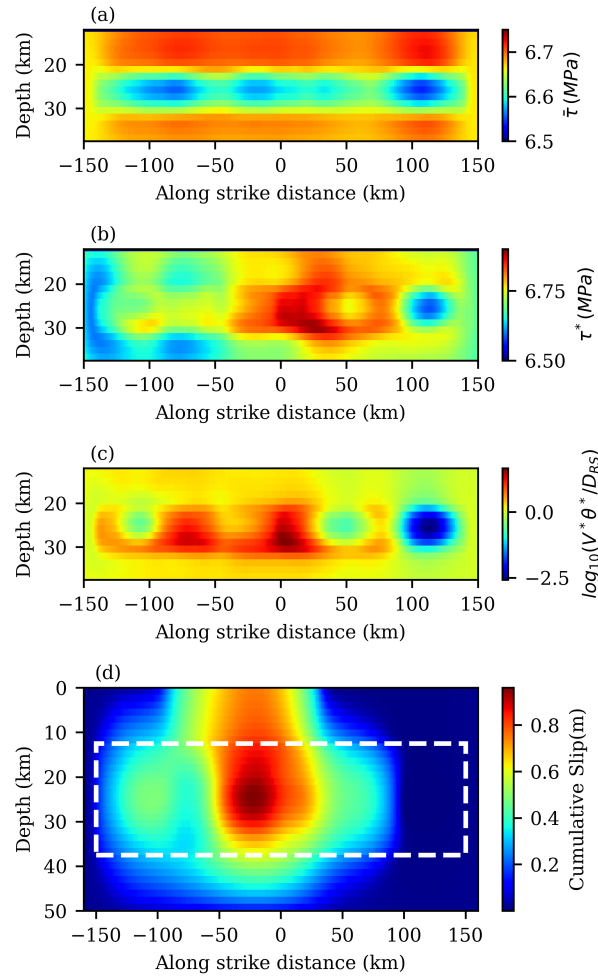


Figure 4. Average of the shear stress on the VW patch of the fault during the interevent period (a). One of the local optimal prestress distributions that leads to an event with a magnitude of 7.5 (b). The dimensionless quantity $\log_{10}(V^*\theta^*/D_{RS})$ for the optimal pre-event V^* and θ^* is plotted in (c). The corresponding cumulative slip of the event that happens right after starting from optimal pre-event state (d). To increase the readability (a,b,c) are plotted only for the VW patch. The VW patch in (d) is denoted by the dashed white line.

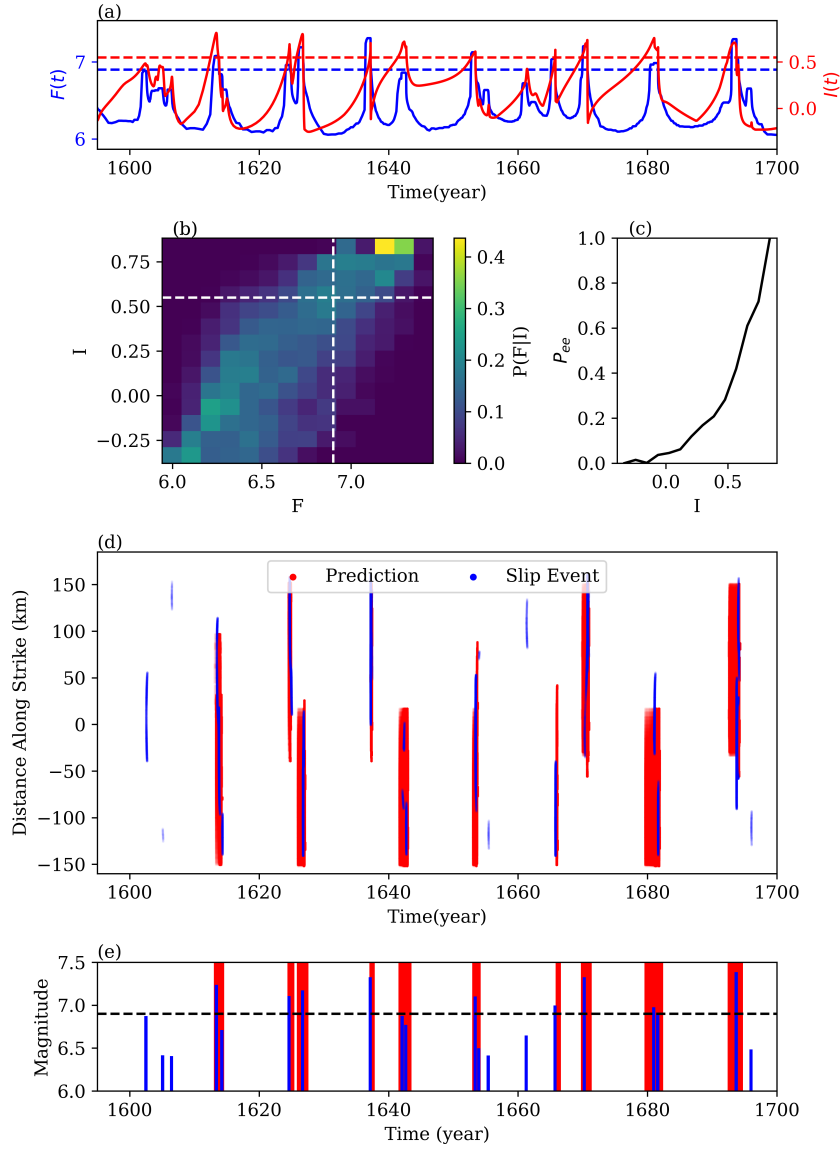


Figure 5. Spatiotemporal prediction of events. The time series of the functions F and I show that I rises when there is an upcoming large event (F is large), and it goes down when there is no upcoming large event. The blue and red dashed lines correspond to F_e and I_e (a). The empirical conditional probability $P(F|I)$. The vertical and horizontal dashed lines are F_e , and I_e respectively (b). The empirical probability of having an event with the value \tilde{M} greater than F_e in the next $0.5(\text{year})$ as a function of the value of the indicator I (c). The spatiotemporal prediction of events is plotted by red where blue is the actual events in the dataset (d). Prediction of the magnitudes with the blue bars as the magnitude of events in the dataset. The horizontal axis for the blue bars denotes the time when an event starts. Red regions denote the times of high probability of large events (above magnitude 6.9 (dashed line)) based on our indicator (e). The statistical plots (b,c) are calculated based on 1000 years of data in the test set (data from the year 1200 to 2200)

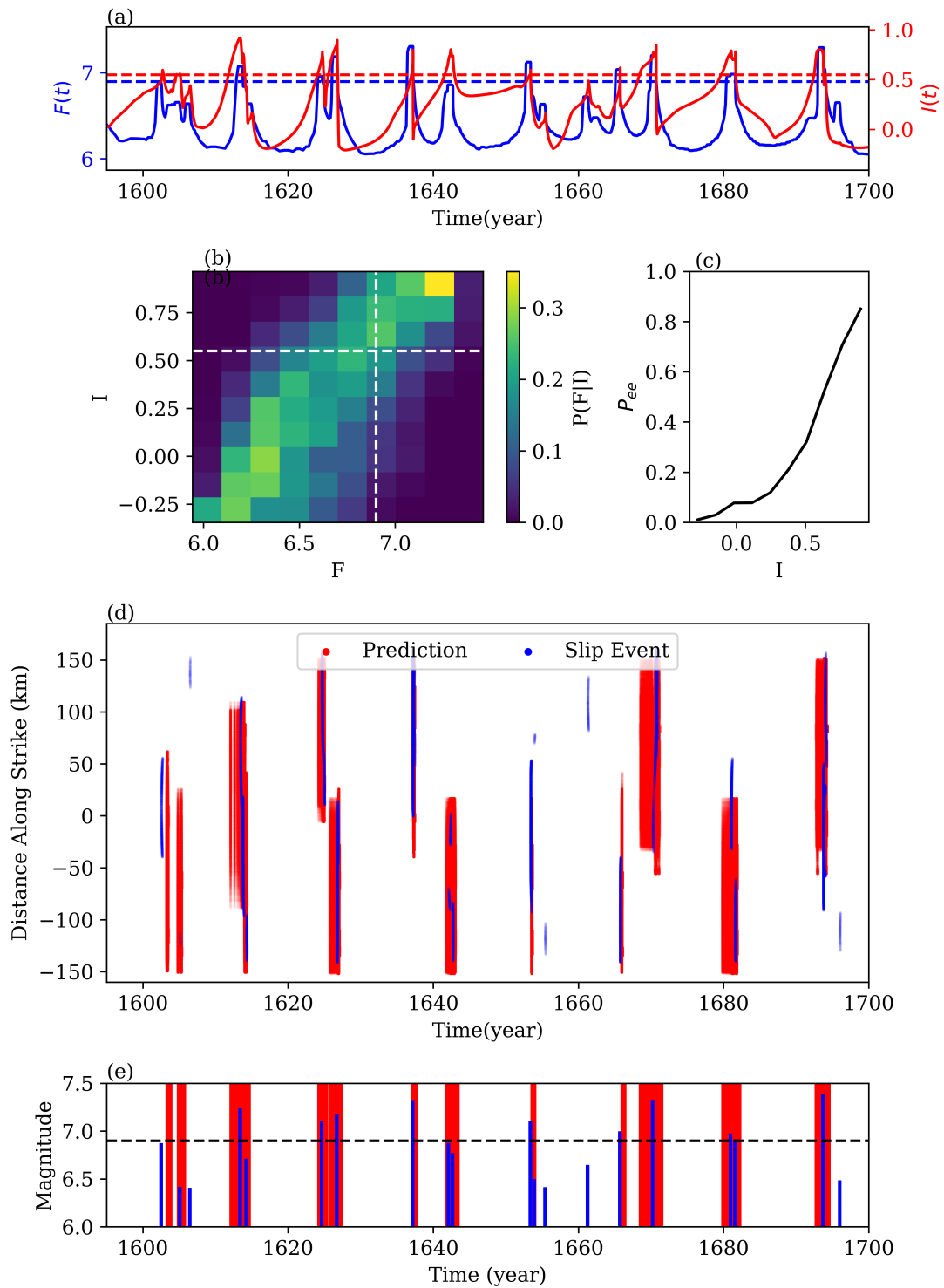


Figure 6. Spatio-temporal prediction of events same as in Fig 5 but using slip rate only at 16 points on the fault (denoted in Fig 1 (a) by diamonds)

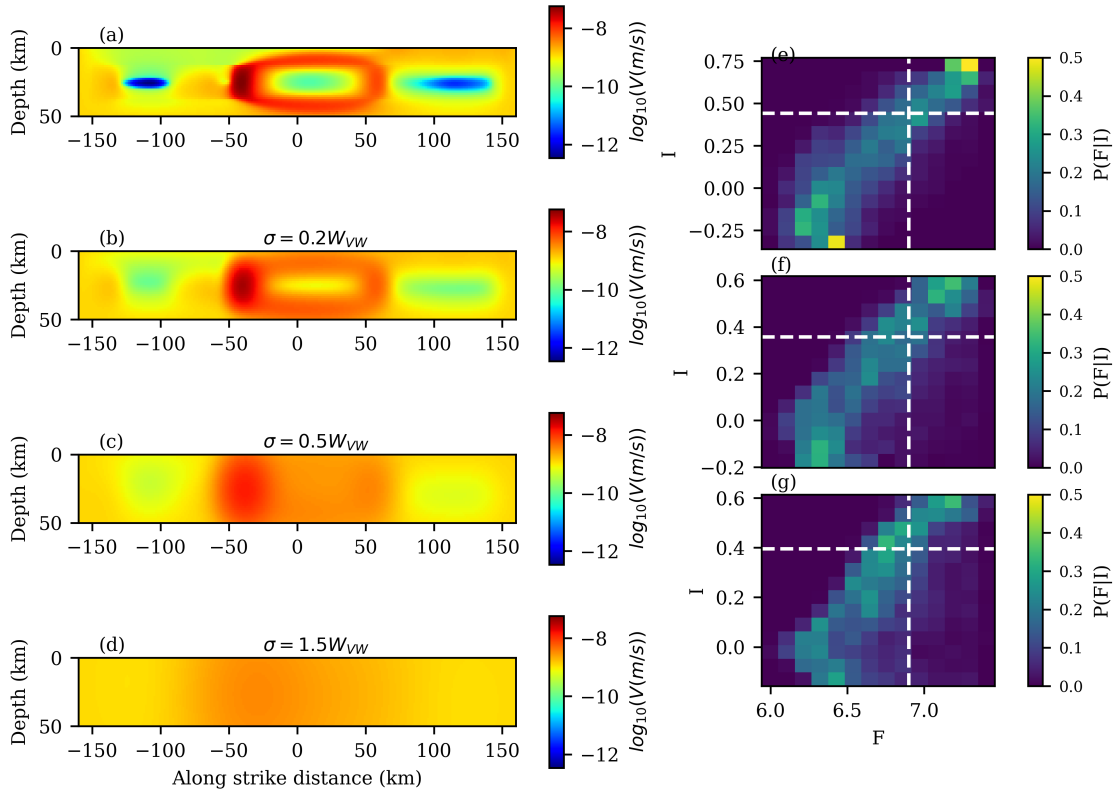


Figure 7. Impact of the lowering the observed slip rate resolution on prediction. One snapshot of the slip rate is plotted in (a). To visualize the effect of reduction of resolution, the low-pass filter applied to the snapshot in (a) is plotted in (b,c,d) with different standard deviations. The conditional probability of $P(F|I)$ when the slip rate is corrupted with a Gaussian low-pass filter with different standard deviations ($\sigma = 0.2W_{VW}, 0.5W_{VW}, 1.5W_{VW}$) are plotted in (e,f,g) respectively.

626 **APPENDIX A: PROPER ORTHOGONAL DECOMPOSITION (POD): METHOD AND**
 627 **RESULT**

628 In this section, we review how to reduce the dimension of the dataset consisting of slip rate and
 629 state variable using the POD method. We use this method to find critical pre-event state in a
 630 low-dimensional space instead of the high-dimensional function space. Another reason to use this
 631 method is because Eq (9) is an optimization problem constrained on the chaotic attractor of the
 632 system with the event period excluded. To solve the constraint optimization problem (Eq (9)), one
 633 method (Farazmand & Sapsis, 2017) is to exclude the extreme events from the chaotic attractor and
 634 approximate the remaining using the POD technique. Here, we exclude the event period from the
 635 dataset to only approximate the interevent period. The method of approximating the chaotic attrac-
 636 tor using POD modes is used in different fields. As an example, the work in (Blonigan et al., 2019)
 637 used 50 POD modes to approximate the chaotic attractor of a turbulent channel flow. One behav-
 638 ioral difference between our model of the earthquake cycle and the turbulent channel flow example
 639 is that the time stepping in our problem is adaptive due to the system’s multi-scale behavior; there
 640 are more sample data when the dynamical system is stiff. However, since we are removing the
 641 event period from the data, we only include the slow part of the system in our dataset.

642 In the following paragraphs, we describe the POD analysis on our dataset of simulations. The data
 643 set comprises snapshots within the time span from the year 200 to 1200 excluding the event set
 644 ($E(V_{\text{thresh}})$). We use the time snapshots of discretized states of the system (θ and V) which be-
 645 long to a high but finite-dimensional space. After discretization, $V : \mathbb{R}^{N_x \times N_y} \times \mathbb{R}^+ \rightarrow \mathbb{R}^+$ and
 646 $\theta : \mathbb{R}^{N_x \times N_y} \times \mathbb{R}^+ \rightarrow \mathbb{R}^+$. $N_x = 256$ and $N_y = 32$ are the numbers of grid points along the strike
 647 and depth respectively.

648 Since the evolution of the system is better realized in \log_{10} space, we apply the POD on the \log_{10}
 649 of the dataset. We define vectors $w_1(t_k)$ and $w_2(t_k)$ both in $\mathbb{R}^{N_x N_z}$ for time t_k as the vectorized

650 form of the logarithm of V and θ at time t_k .

$$w_1(t_k) = \log_{10} \begin{pmatrix} V_{1,1} \\ V_{1,2} \\ \vdots \\ V_{1,N_x} \\ V_{2,1} \\ V_{2,2} \\ \vdots \\ V_{2,N_x} \\ \vdots \\ V_{N_z,1} \\ V_{N_z,2} \\ \vdots \\ V_{N_z,N_x} \end{pmatrix}_{t=t_k} \tag{A.1}$$

$$w_2(t_k) = \log_{10} \begin{pmatrix} \theta_{1,1} \\ \theta_{1,2} \\ \vdots \\ \theta_{1,N_x} \\ \theta_{2,1} \\ \theta_{2,2} \\ \vdots \\ \theta_{2,N_x} \\ \vdots \\ \theta_{N_z,1} \\ \theta_{N_z,2} \\ \vdots \\ \theta_{N_z,N_x} \end{pmatrix}_{t=t_k} \tag{A.2}$$

651 where for example, by $[V_{i,j}]_{t_k}$, we mean slip rate at i^{th} element along strike and j^{th} element along
 652 the depth at k^{th} snapshots in the dataset. Then, we stack pairs of w_1 and w_2 to make a vector w :

$$w(t_k) = \begin{bmatrix} w_1(t_k) \\ w_2(t_k) \end{bmatrix} \in \mathbb{R}^{2N_x N_z}. \quad (\text{A.3})$$

653 We define $\bar{w} = [\bar{w}^V, \bar{w}^\theta]^\top$ as the time average of $w(t_i)$ for all i in the dataset.

$$\bar{w} = \frac{1}{N_d} \sum_{i=1}^{N_d} w(t_i) \quad (\text{A.4})$$

654 where N_d is the total number of snapshots in the dataset. \bar{w}^V and \bar{w}^θ are plotted in Fig 3. We define
 655 $p(t_k) = w(t_k) - \bar{w}$ and then we define a matrix $P \in \mathbb{R}^{2N_x N_z \times N_d}$ with the following entries:

$$P = [p(t_1) \ p(t_2) \ \cdots \ p(t_{N_d})] \in \mathbb{R}^{2N_x N_z \times N_d}. \quad (\text{A.5})$$

656 Then, we define the covariance matrix R as the following:

$$R = \frac{1}{(N_d - 1)} P P^T \in \mathbb{R}^{2N_x N_z \times 2N_x N_z} \quad (\text{A.6})$$

657 Now, we can find the eigenvectors of matrix R :

$$R\phi_j = \lambda_j \phi_j \quad \lambda_1 \geq \lambda_2 \geq \cdots \geq \lambda_{2N_x N_z} \geq 0. \quad (\text{A.7})$$

658 Eigenvalues show how well each eigenvector captures the original data in L^2 sense. Eigen-vectors
 659 of matrix R can be found using Singular Value Decomposition (SVD) of matrix P :

$$P = \Phi \Sigma \Psi^T \quad (\text{A.8})$$

660 where in general $\Phi \in \mathbb{R}^{2N_x N_y \times 2N_x N_y}$ and $\Psi \in \mathbb{R}^{N_d \times N_d}$ are orthogonal ($\Phi \Phi^T = I_{2N_x N_y \times 2N_x N_y}$ and
 661 $\Psi \Psi^T = I_{N_d \times N_d}$) and determine, through columns, the left and right singular vectors of P ; and
 662 diagonal matrix $\Sigma \in \mathbb{R}^{2N_x N_y \times N_d}$ has singular values on its diagonal (Taira et al., 2017). We can
 663 write:

$$R = \frac{1}{(N_d - 1)} P P^T = \frac{1}{(N_d - 1)} \Phi \Sigma \Psi^T \Psi \Sigma^T \Phi^T$$

$$R\Phi = \frac{1}{(N_d - 1)} \Phi \Sigma \Sigma^T \quad (\text{A.9})$$

665 because of the special form of Σ that will be discussed shortly, the columns of Φ (denoted here by
 666 ϕ_i and are plotted in Fig 3 for $i \leq 4$) are eigenvectors of matrix R that are ordered by the variance

667 they capture in data. Note that $\phi_i \in \mathbb{R}^{2N_x N_y}$ and we can separate it into eigenvectors of the slip
 668 rate (ϕ_i^V) and the state variable ϕ_i^θ :

$$\phi_i = \begin{bmatrix} \phi_i^V \\ \phi_i^\theta \end{bmatrix} \quad (\text{A.10})$$

669 Assuming the number of time snapshots is much smaller than the dimension of the problem
 670 $N_d \ll 2N_x N_y$, Σ has the following form:

$$\Sigma = \begin{bmatrix} \sigma_1 & 0 & 0 & 0 \\ 0 & \sigma_2 & 0 & 0 \\ \vdots & \vdots & \ddots & \vdots \\ 0 & 0 & 0 & \sigma_{N_d} \\ 0 & 0 & 0 & 0 \\ \vdots & \vdots & \vdots & \vdots \\ 0 & 0 & 0 & 0 \end{bmatrix}_{2N_x N_y \times N_d} \quad (\text{A.11})$$

671 Then, using Eqs (A.7), (A.9), and (A.11), $\frac{1}{(N_d-1)}\sigma_j^2 = \lambda_j$. λ_j corresponds to the variance of the
 672 data along ϕ_j . If λ_j goes to zero very fast, it suggests that we can explain the dataset in a low-
 673 dimensional subspace consisting of a finite number of eigenfunctions. The ratio $\sum_{j=1}^r \lambda_j / \sum_{j=1}^{N_d} \lambda_j$
 674 shows the proportion of the variance of the data that are captured in the first r eigenfunctions.
 675 Based on Fig A1, the first 13 modes of the data capture almost 85% of the data.

676 Using this explanation, we can approximate the interevent period ($\mathcal{A} \setminus E(V_{\text{thresh}})$) by:

$$\log_{10}(\mathcal{A} \setminus E(V_{\text{thresh}})) \approx \left\{ w = \bar{w} + \sum_{i=1}^{N_m} a_i \phi_i \mid \sum_{i=1}^{N_m} \frac{a_i^2}{\lambda_i} \leq r_0^2 \right\}. \quad (\text{A.12})$$

677 where N_m is the number of modes (eigenfunctions) that are considered in the truncation. One
 678 can play with r_0 to enlarge the set. For very large r_0 the approximation is not valid anymore. The
 679 value of r_0 determines how much we let perturbation around the average of the dataset \bar{w} . As an
 680 example, taking $N_m = 1$ and $r_0 = 1$ would let perturbation around \bar{w} along ϕ_1 with an amplitude
 681 equal to the standard deviation of the dataset along that eigenvector ($\sqrt{\lambda_1}$).

682 Using the orthonormality of ϕ_i 's, we can find the projection of any $w(t)$ onto ϕ_i using the
683 following inner product:

$$a_i(t) = \langle w(t) - \bar{w}, \phi_i \rangle \quad (\text{A.13})$$

684 where $a_i(t)$ is the projection of $w(t) - \bar{w}$ onto eigenvector ϕ_i and \langle, \rangle denotes the inner product.
685 We can find $a_i(t_k)$ for all of the time snapshots in the dataset and plot the distribution of $a_i/\sqrt{\lambda_i}$
686 (Fig A2). We see that the distribution is close to the standard normal distribution. Looking at this
687 figure gives us intuition about choosing a value for r_0 . For example, selecting r_0 to be large (> 4),
688 would lead to exploring low-probability regions. The dashed lines in the figure, correspond to
689 $a_i/\sqrt{\lambda_i} = 1, 2, 3$.

690 Using the approximation in Eq (A.12), we reduce the dimensionality of the system from
691 $\mathbb{R}^{2N_x N_z}$ to \mathbb{R}^{N_m} and approximate a complicated set ($\mathcal{A} \setminus E(V_{\text{thresh}})$) by a hyperellipse which is
692 a straightforward constraint for our optimization problem. With the mentioned approximation,
693 and denoting $w^* = \bar{w} + \sum_{i=1}^{N_m} a_i^* \phi_i$, we write an optimization problem in the low dimensional
694 \mathbb{R}^{N_m} space which is an equivalent approximate of Eq (9):

$$A^* = \{\mathbf{a}^* \mid \sum_{i=1}^{N_m} \frac{a_i^{*2}}{\lambda_i} \leq r_0^2, w^* \text{ is a local maximizer of } F(10^{w^*}; \Delta t, T), F(10^{w^*}; \Delta t, T) > F_e^*\} \quad (\text{A.14})$$

695 where $\mathbf{a}^* \in \mathbb{R}^{N_m}$ whose i^{th} element is a_i^* . Eq (A.14) ensures that the optimal solutions are not too
696 far from the mean states (\bar{w}).

697 To show the applicability of the POD model reduction outside the application of this paper, we
698 also applied the method to a dataset including all snapshots within the period of 200 years to
699 1200 years (without removing the event period). The result of this model reduction is available in
700 Supplemental Video 2. This video shows that we can capture all phases of earthquake cycles using
701 a few POD modes.

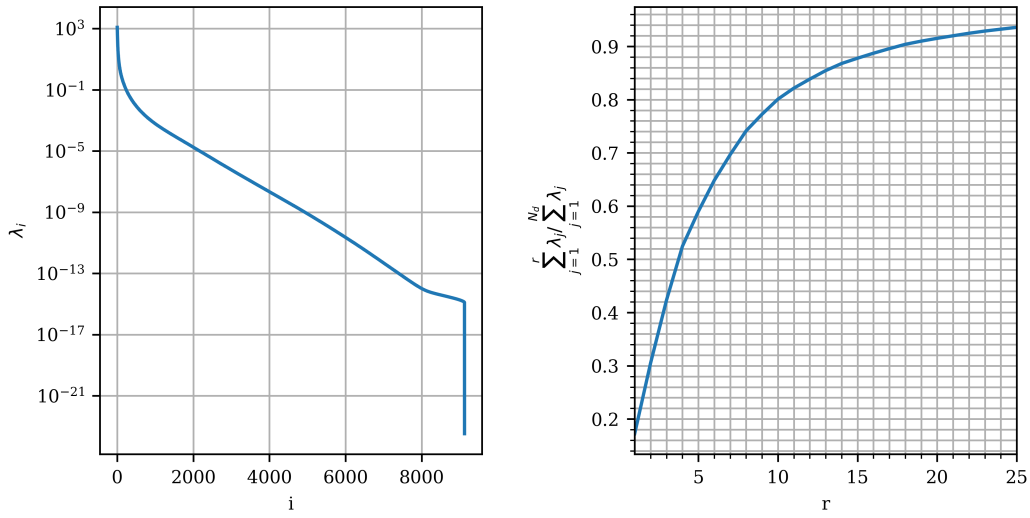


Figure A1. Convergence of the eigenvalues (left) and the ratio of a truncated sum of eigenvalues to the total sum of eigenvalues (right).

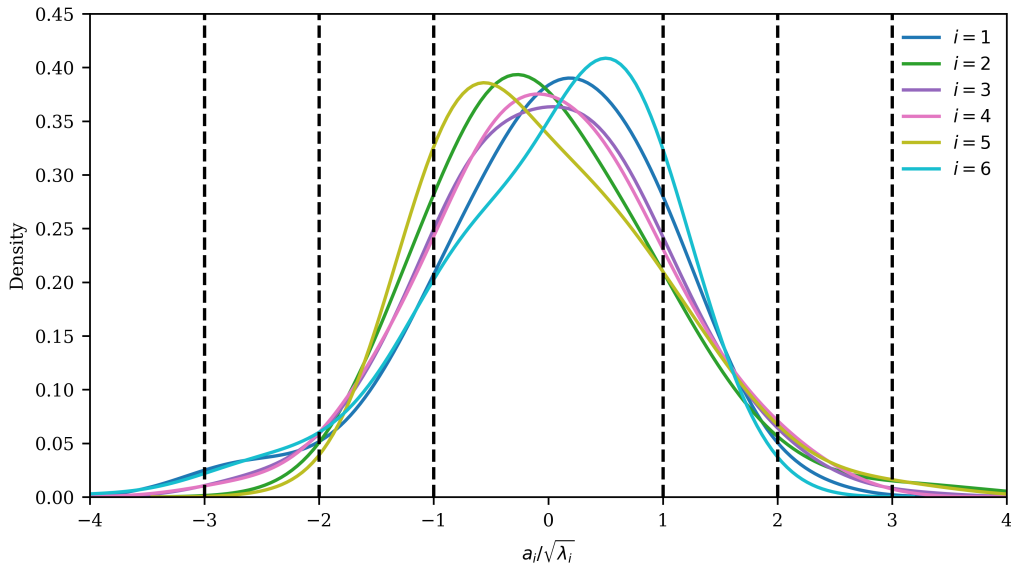


Figure A2. The distribution of $a_i(t)/\sqrt{\lambda_i}$ in the dataset of the interevent periods. The vertical lines correspond to $a_i/\sqrt{\lambda_i} = \pm 1, \pm 2, \pm 3$ and are plotted to give insight for selecting proper r_0 in Eq (10)

702 **APPENDIX B: OPTIMIZATION**

703 Here we revisit optimal sampling in the framework of Bayesian optimization as discussed in
 704 (Brochu et al., 2010) and is improved in (Blanchard & Sapsis, 2021) for finding the precu-
 705 sors of extreme events. The optimization algorithm works by exploring the input space ($\mathbf{a} =$
 706 $[a_1, \dots, a_{N_m}] \in \mathbb{R}^{N_m}$) using a Gaussian surrogate model. Suppose that we want to solve the con-
 707 strained optimization problem of Eq (9) with the approximation in Eq (10). Without loss of gen-
 708 erality, we study the minimization of the minus sign of the cost function ($G = -F$) instead of
 709 maximizing it. The cost function can be evaluated using a forward simulation of a given initial
 710 condition. Here we assume that the observation is contaminated by a small Gaussian noise with
 711 variance $\sigma_\epsilon^2 = 10^{-4}$.

$$z = G(a; T, \Delta t) + \epsilon \quad \epsilon \sim \mathcal{N}(0, \sigma_\epsilon^2) \quad (\text{B.1})$$

712 where ϵ is the observational noise, and T and Δt are hyperparameters of the cost function G that
 713 are determined before the optimization process. The iterative approach starts from some randomly
 714 sampled N_{init} points $\{\mathbf{a}_k \in \mathbb{R}^{N_m}\}_{k=1}^{N_{init}}$ that each of them corresponds to a point in the set defined
 715 in (10). Using the forward model of Eq (B.1) we find the input-output pair $\mathcal{D}_0 = \{\mathbf{a}_k, z_k\}_{k=1}^{N_{init}}$.
 716 $\mathbf{a}_k \in \mathbb{R}^{N_m}$ is the vector of POD coefficients with N_m as the number of POD modes we have
 717 decided to consider, and z_k comes from Eq (B.1). Using a Gaussian surrogate model, the expected
 718 value and variance of the process, condition on the input/output at each step i (\mathcal{D}_i) is given by the
 719 following equation:

$$\begin{aligned} \mu(\mathbf{a}) &= m_0 + k(\mathbf{a}, \mathbf{A}_i) \mathbf{K}_i^{-1} (\mathbf{z}_i - m_0) \\ \sigma^2(\mathbf{a}) &= k(\mathbf{a}, \mathbf{a}) - k(\mathbf{a}, \mathbf{A}_i) \mathbf{K}_i^{-1} k(\mathbf{A}_i, \mathbf{a}) \end{aligned} \quad (\text{B.2})$$

720 where $\mathbf{K}_i = k(\mathbf{A}_i, \mathbf{A}_i) + \sigma_\epsilon^2 \mathbf{I}$, $\mathbf{A}_i = \{\mathbf{a}_k\}_{k=1}^{N_{init}+i}$, and $\mathbf{z}_i = \{z_k\}_{k=1}^{N_{init}+i}$. We consider the Radial
 721 Basis Function (RBF) with Automatic Relevance Determination (ARD):

$$k(\mathbf{a}, \mathbf{a}') = \sigma_f^2 \exp(-(\mathbf{a} - \mathbf{a}')^T \Theta^{-1} (\mathbf{a} - \mathbf{a}') / 2) \quad (\text{B.3})$$

722 where Θ is a diagonal matrix containing the length scale for each dimension. At each iteration,
 723 we construct a surrogate model (Eq (B.2)). Then, the next point in the input space is found by

724 minimizing an acquisition function ($g : \mathbb{R}^{N_m} \rightarrow \mathbb{R}$). We use the **Lower Confidence Bound**
 725 (LCB) acquisition function which is defined as the following:

$$g_{LCB}(\mathbf{a}) = \mu(\mathbf{a}) - \kappa\sigma(\mathbf{a}) \quad (\text{B.4})$$

726 where κ is a positive number that balances exploration and exploitation. For small κ , we do not
 727 consider uncertainties of the surrogate model and trust the mean of the conditional Gaussian pro-
 728 cess. For large κ , minimizing Eq (B.4) is equivalent to finding a point that has the largest uncer-
 729 tainty. We use $\kappa = 1$ in this study. The algorithm is extracted from Ref (Blanchard & Sapsis, 2021)
 730 and is summarized in Algorithm 1. We start the algorithm by randomly sampling 10 initial points
 731 inside the hyper-ellipse (Eq (10)) and then augmenting the input-output pairs by minimizing the
 732 acquisition function until the size of the input-output points reaches 200. To show the effectiveness
 733 of the algorithm in finding optimal solutions, we define the function c as the following:

$$c(i) = - \min_{1 \leq j \leq i} \min_{\mathbf{a}} \mu(\mathbf{a} | \mathcal{D}_j) \quad (\text{B.5})$$

734 To find $c(i)$, we need to find the minimum of the Gaussian process in each iteration i and report the
 735 minimum over all $1 \leq j \leq i$. The algorithm does not guarantee finding all of the local maxima. As
 736 a result, the algorithm is repeated for 30 trials with different randomly chosen initial points. The
 737 behaviour of $c(i)$ for different values of r_0 is plotted in Fig B1 (a). The solid line is the median
 738 of $c(i)$ for different trials as a function of iteration and the shaded band shows half of the median
 739 absolute deviation. One of the optimal solutions is plotted in Fig B1 (b,c). During the optimization
 740 process, we augment the set W^* if the condition in Eq (11) is satisfied.

Algorithm 1 Bayesian Optimization

- 1: **Input:** Number of initial points n_{init} and number of iterations n_{iter}
- 2: **Initialize:** Surrogate model on initial dataset $\mathcal{D}_0 = \{\mathbf{a}^{(k)}, z^{(k)}\}_{k=1}^{n_{init}}$
- 3: **for** $n=0$ to n_{iter} **do**
- 4: Select best next point \mathbf{a}_{n+1} by minimizing acquisition function constrained inside the hyperellipse (Eq (10)):

$$\mathbf{a}^{(n+1)} = \arg \min_{\sum_{i=1}^{N_m} \frac{a_i^2}{\lambda_i} \leq r_0^2} g_{LCB}(\mathbf{a}; \bar{G}, \mathcal{D}_n)$$

- 5: Evaluate objective function G at $\mathbf{a}^{(n+1)}$ and record $z^{(n+1)}$
- 6: If $z^{(n+1)} < -F_e^*$ augment the set W^* (Eq (11))
- 7: Augment dataset $\mathcal{D}_{n+1} = \mathcal{D}_n \cup \{\mathbf{a}_{n+1}, z_{n+1}\}$
- 8: Update surrogate model
- 9: **end for**

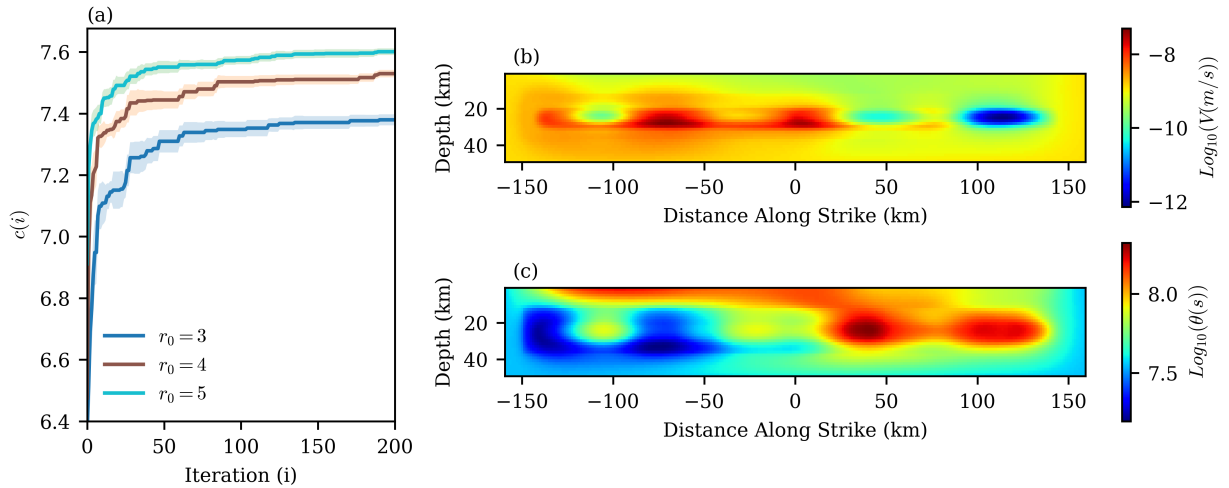


Figure B1. Convergence of the optimization for different values of r_0 (a). $\log_{10}(V)$ and $\log_{10} \theta$ of one of the optimal solutions with $r_0 = 3$ which leads to a magnitude 7.5. The optimal solution is highly heterogeneous and shows the effect of favorable stress heterogeneity in generating big events (b,c). The stress calculated from this optimal solution is plotted in Fig 4